

Chapter 8

Optical capture and manipulation of micro- and nano-objects

The optical capture and rotation of microobjects are based on the well-known phenomenon of light pressure. After developing lasers it became possible to generate the radiation pressure force sufficient for acceleration, deceleration, deflection, direction and stable capture of microscopic objects, whose dimensions range from tens of nanometers to tens of micrometers. If the refractive index is greater than the refractive index of the medium, the force resulting from changes in the direction of the light acts on the micro-object so that it moves into the region of the highest light intensity.

The first experiments with the capture and acceleration of micro-objects, suspended in liquid and gas, are described in [30]. In 1977, changes were detected in the force of radiation pressure on the transparent dielectric spherical objects, depending on the wavelength and size [31].

If the first studies it was shown that a micro-object can be captured and moved linearly, then subsequent studies considered the possibility of rotating and orienting micro-objects in space. Optical rotation allows non-contact drives for micromechanical systems [58], also has many applications in biology [85]

There are three main ways of rotation of microscopic objects.

- Due to the spin angular momentum, which exists in the fields with circular polarization. In this case only the birefringent micro-objects, such as micro-objects made of Iceland spar, rotate [35, 36]. The main drawback of this method is the restriction on the material from which the micro-object is made.

- Due to the orbital angular momentum, which arises due to the spiral shape of the wave front, such as Laguerre–Gaussian (LG) and Bessel beams of higher orders. Transfer of the orbital angular momentum is due to partial absorption of light in the micro-object. This method is presented in [37, 50, 58]. In these studies, Bessel LG beams formed with the use of amplitude holograms, which is unprofitable from the standpoint of energy efficiency. It is much more efficient to use pure phase DOEs, for example to create Bessel beams (BB) [65]. There are works in which the micro-objects move along paths other than the circle, for example, a light triangle, square, spiral [5, 23–26].

– By changing the phase shift in the interference pattern (in capture of a microscopic object in the interference pattern) between the beam having a helical wavefront (i.e., LG beam) and the Gaussian beam. This pattern is rotated by changing the optical path length of one of the beams. This method is described in [82]. The main drawback of this method is the need to use a fairly complex optical circuit. In this case it is also easier to use the DOE that forms a superposition of Bessel of LG modes [11]. Rotating BB or LG which in propagation along the optical axis is accompanied by the rotation of the intensity distribution in the beam cross section can be used to rotate microscopic objects with variable speed by using the linear displacement of the radiation source or a focusing lens. In this case, the optical system is reduced, in fact, to one DOE.

2D-arrays of traps (micro-objects are pressed to the table of the microscope) have potential application for building elements of micro-optomechanical systems [49, 59], the formation of different micro-configurations [60], the sorting of biological cells [54] and other applications that do not require manipulation of longitudinal objects.

A system of two traps was realized with the help of a beam splitter and refractive optics [46, 84]. However, this approach is very complicated if a larger number of traps is required. An alternative and more promising approach is the separation and guiding of the laser beam with the DOE [37, 42, 43, 53, 56].

In [38] the authors proposed to supplement a dynamic diffractive element, which is a matrix of $N \times N$ programmable phase gratings, with a $N \times N$ matrix of microlenses. In [37] the iterative method was used for calculating the phase DOE for creating 2D and 3D arrays of optical traps. In the experiments, the matrix was formed from eight Gaussian beams. The main disadvantage of spatial light modulators based on liquid crystals remain low diffraction efficiency (strong diffraction noise due to the high discreteness of the modulators) and the insufficient resolution of the matrix of pixels to handle the complex phase distributions. Also, the final pixel size limits the maximum variation of the diffraction orders (high carrier spatial frequencies are accompanied by the binarization of the phase profile and diffraction efficiency decreases).

Measurements have shown [79] that 15% of the energy of the incident beam remains after the liquid crystal modulator. Energy losses are due to several reasons:

- 1) the opaque part of the panel (core loss, up to 65%),
- 2) the structure of the liquid crystal modulator is similar to the grating, generating high orders (54% loss),
- 3) the inability to concentrate all the energy in a useful manner, because the modulator has a maximum phase shift of less than 2π (maximum ratio achieved between the first and zero order of 2:1) [79],
- 4) the discrepancy between the square aperture of the panel and the round profile of the incident beam (8%). Thus, the use of DOE for the formation of multiorder light beams for micro-object rotation problems if no dynamics is required, is preferred to the use of dynamic light modulators.

There are many studies in which solutions with separable variables for the Helmholtz and Schrödinger equations are used in optics. These studies examined multimode Bessel beams [57], multiorder LG beams [21], non-paraxial light beams that retain their structure during propagation [33], parabolic beams, Gauss-Helmholtz waves, paraxial light beams that retain their structure up to scale, Ince-Gaussian modes [33], elegant Ince-Gaussian beams [33], Hermite-Laguerre-Gaussian modes [22], optical vortices [66]. Some of these beams have been realized with laser resonators [66], liquid crystal displays [34, 87], phase DOEs [57, 67, 68]. These beams can provide additional new features in the problem of ‘optical tweezers’.

There is a considerable number of works [13, 29, 32, 41, 51, 72, 74, 77, 78, 80, 83] concerned with the calculation of forces acting on the micro-object. In the well-known papers on the calculation of forces acting on the micro-object using the geometric optics approach, restrictions are imposed on the shape of the micro-object and the shape of the beam, and, as a rule, the motion parameters of the micro-object are not considered. For example, in [29] the authors considered only spherical micro-objects in a Gaussian beam. In [51], the force was calculated for the non-spherical micro-objects, but the authors consider the case of a Gaussian beam. In [13] the spherical and elliptical Gaussian beams in micro-objects Gaussian and LG beams were considered.

8.1. Calculation of the force acting on the micro-object by a focused laser beam

This section describes the derivation of the expressions for the force acting on a two-dimensional dielectric cylindrical two-dimensional object from a monochromatic electromagnetic wave.

8.1.1. Electromagnetic force for the three-dimensional case

In [1] a formula is derived which expresses the conservation of the total momentum of the system of the electromagnetic field plus the object V , bounded by the surface S :

$$\frac{\partial}{\partial t} \int_{V_1} P_i dV + \frac{\partial}{\partial t} P_{0i} = - \oint_{S_1} \sigma_{ik} n_k dS, \quad (8.1)$$

where P_i are the coordinates of the vector of the momentum of the electromagnetic field (V_1 and S_1 are the volume and the surface restricting it, which include an object $V \in V_1$) that is associated with the Umov-Poynting vector by the relation:

$$\mathbf{P} = \frac{\mathbf{S}}{c} = \frac{1}{4\pi c} [\mathbf{E} \times \mathbf{H}], \quad (8.2)$$

P_{0i} are the coordinates of the momentum vector of the object, $\delta P_{0i} / \delta t$ are the coordinates of the force vector of the light on the object ($\mu = 1$):

$$\sigma_{ik} = \frac{1}{4\pi} \left(\frac{|\mathbf{E}|^2 + |\mathbf{H}|^2}{2} \delta_{ik} - E_i E_k - H_i H_k \right); \quad (8.3)$$

σ_{ik} is the Maxwell stress tensor of the electromagnetic field ($\sigma_{ik} = \sigma_{ki}$); \mathbf{E} , \mathbf{H} are the vectors of the strength of the electric and magnetic fields in a vacuum.

After averaging over the time period of $T = 2\pi/\omega$ of the monochromatic light:

$$\mathbf{E}(\mathbf{x}, t) = \text{Re} \left\{ \mathbf{E}(\mathbf{x}) e^{i\omega t} \right\}, \quad \mathbf{H}(\mathbf{x}, t) = \text{Re} \left\{ \mathbf{H}(\mathbf{x}) e^{i\omega t} \right\} \quad (8.4)$$

instead of equation (8.1) we get:

$$F_i = \left\langle \frac{\partial P_{0i}}{\partial t} \right\rangle = - \oint \langle \sigma_{ik} \rangle n_k dS, \quad (8.5)$$

as

$$\left\langle \frac{\partial}{\partial t} \int_V P_i dV \right\rangle = \int_V \left\langle \frac{\partial}{\partial t} P_i \right\rangle dV = 0. \quad (8.6)$$

It can be shown that:

$$\begin{aligned} \left\langle \frac{\partial P_x}{\partial t} \right\rangle &= \frac{1}{4\pi c} \left\{ \left\langle \text{Re} \left(i\omega E_y(\vec{x}) e^{i\omega t} \right) \text{Re} \left(H_z(\vec{x}) e^{i\omega t} \right) \right\rangle + \right. \\ &\quad \left. + \left\langle \text{Re} \left(E_y(\vec{x}) e^{i\omega t} \right) \text{Re} \left(i\omega H_z(\vec{x}) e^{i\omega t} \right) \right\rangle - \right. \\ &\quad \left. - \left\langle \text{Re} \left(i\omega E_z(\vec{x}) e^{i\omega t} \right) \text{Re} \left(H_y(\vec{x}) e^{i\omega t} \right) \right\rangle - \right. \\ &\quad \left. - \left\langle \text{Re} \left(E_z(\vec{x}) e^{i\omega t} \right) \text{Re} \left(i\omega H_y(\vec{x}) e^{i\omega t} \right) \right\rangle \right\} = 0, \quad (8.7) \end{aligned}$$

where $\text{Re}(\dots)$ - the real part of complex number $\langle f(t) \rangle = \frac{1}{T} \int_0^T f(t) dt$. Similarly to

(8.7) for the other projections of the momentum vector of the electric field it can be

shown that $\left\langle \frac{\partial P_y}{\partial t} \right\rangle = \left\langle \frac{\partial P_z}{\partial t} \right\rangle = 0$.

To obtain expressions for the time-averaged stress tensor (3) we take into account that

$$\left\langle \text{Re} \left(E_i(\vec{x}) e^{i\omega t} \right) \text{Re} \left(E_j(\vec{x}) e^{i\omega t} \right) \right\rangle = \frac{1}{2} \text{Re} \left[E_i(\vec{x}) E_j^*(\vec{x}) \right]. \quad (8.8)$$

Then instead of (8.5) we obtain (ε_2 is the dielectric constant of the medium):

$$\begin{aligned}
F_x &= \frac{1}{8\pi} \oint_s \left\{ \frac{1}{2} [\varepsilon_2 |E_x|^2 + |H_x|^2 - \varepsilon_2 |E_y|^2 - \right. \\
&\quad \left. - |H_y|^2 - \varepsilon |E_z|^2 - |H_z|^2] dS_x + \right. \\
&\quad \left. + \operatorname{Re}(\varepsilon_2 E_x E_y^* + H_x H_y^*) dS_y + \operatorname{Re}(\varepsilon_2 E_x E_z^* + H_x H_z^*) dS_z \right\}, \\
F_y &= \frac{1}{8\pi} \oint_s \left\{ \frac{1}{2} [\varepsilon_2 |E_y|^2 + |H_y|^2 - \varepsilon_2 |E_x|^2 - \right. \\
&\quad \left. - |H_x|^2 - \varepsilon_2 |E_z|^2 - |H_z|^2] dS_y + \right. \\
&\quad \left. + \operatorname{Re}(\varepsilon_2 E_y E_z^* + H_y H_z^*) dS_z + \operatorname{Re}(\varepsilon_2 E_y E_x^* + H_y H_x^*) dS_x \right\}, \\
F_z &= \frac{1}{8\pi} \oint_s \left\{ \frac{1}{2} [\varepsilon_2 |E_z|^2 + |H_z|^2 - \varepsilon_2 |E_x|^2 - \right. \\
&\quad \left. - |H_x|^2 - \varepsilon_2 |E_y|^2 - |H_y|^2] dS_z \right. \\
&\quad \left. + \operatorname{Re}(\varepsilon_2 E_z E_x^* + H_z H_x^*) dS_x + \operatorname{Re}(\varepsilon_2 E_z E_y^* + H_z H_y^*) dS_y \right\}, \tag{8.9}
\end{aligned}$$

where $dS_x = -\frac{\partial z}{\partial x} dx dy$, $dS_y = \frac{\partial z}{\partial y} dx dy$, $dS_z = dx dy$, $E_1 = E_x$, $E_2 = E_y$, $E_3 = E_z$ (and similarly for H_i and F_i).

8.1.2 Electromagnetic force for the two-dimensional case

We rewrite the expression (8.9) for the force of the action of light on the micro-object in the 2D case. For the TE-polarization ($H_x = E_y = E_z = 0$) the electric field is directed along the axis X , $E_x \neq 0$, Z is the optical axis, the 2D-object has the form of a cylinder with the arbitrary cross-sectional shape and has an infinite length along the axis X . The plane YOZ is the plane of incidence. In this case the relation (8.9) takes the form:

$$\begin{aligned}
F_x &= 0, \\
F_y &= \frac{1}{8\pi} \oint_{S_1} \left\{ \frac{1}{2} [|H_y|^2 - \varepsilon_2 |E_x|^2 - |H_z|^2] dS_y + \operatorname{Re}(H_y H_z^*) dS_z \right\}, \tag{8.10} \\
F_z &= \frac{1}{8\pi} \oint_{S_1} \left\{ \frac{1}{2} [|H_z|^2 - \varepsilon_2 |E_x|^2 - |H_y|^2] dS_z + \operatorname{Re}(H_z H_y^*) dS_y \right\},
\end{aligned}$$

Here S_1 is already a contour enclosing a section of the object in the plane YOZ . Force F_2 is directed along the optical axis and is analogous to the scattering force for the Rayleigh particles [2], and F_y is directed across the optical axis and is analogous to the gradient force [2]. The relationship between the projections H_y , H_z and E_x (TE-polarization) follows from Maxwell's equations:

$$H_y = \frac{i}{k_0 \mu} \frac{\partial E_x}{\partial z}, H_z = \frac{1}{ik_0 \mu} \frac{\partial E_x}{\partial y}, \quad (8.11)$$

between the projections E_y , E_z and H_x , and (TM-polarization):

$$E_y = \frac{1}{ik_0 \varepsilon} \frac{\partial H_x}{\partial z}, E_z = \frac{i}{k_0 \varepsilon} \frac{\partial H_x}{\partial y}, \quad (8.12)$$

where $k_0 = 2\pi/\lambda$ is the wavenumber of light with a wavelength λ , ε is the dielectric constant of the medium, μ is the magnetic permeability of the medium. Similar to (8.10), the force of light pressure with TM-polarization for the 2D object will have the following projections ($E_x = H_y = H_z = 0$):

$$F_x = 0,$$

$$F_y = \frac{1}{8\pi} \oint_{S_1} \left\{ \frac{1}{2} \left[\varepsilon_2 |E_y|^2 - \varepsilon_2 |E_z|^2 - |H_x|^2 \right] dS_y + \varepsilon_2 \operatorname{Re} \left(E_y E_z^* \right) dS_z \right\}, \quad (8.13)$$

$$F_z = \frac{1}{8\pi} \oint_{S_1} \left\{ \frac{1}{2} \left[\varepsilon_2 |E_z|^2 - \varepsilon_2 |E_y|^2 - |H_x|^2 \right] dS_z + \varepsilon_2 \operatorname{Re} \left(E_z E_y^* \right) dS_y \right\},$$

where (as in equation (8.10)) $dS_y = n_y dl = \sin \phi dl = dz$ and $dS_z = n_z dl = \cos \phi dl = dy$ and dl is the element of arc.

8.1.3. Calculation of force for a plane wave

To calculate the force exerted by the light field on a cylindrical object, we must calculate the integral over the contour within which the object resides. As follows from the formulas for calculating the force projections (8.10), (8.13), the force should not change when the radius of integration R_i changes, if the object is completely enclosed in the integration contour: $R_i > R$.

We calculate the iterative algorithm of the diffraction field of a plane wave on a cylindrical object, and we also calculate the force acting on it at various radii of integration. Simulation parameters: the incident wave is flat, the entire calculated diffraction field $10 \times 10 \mu\text{m}$, the wavelength $1 \mu\text{m}$. The object is a cylinder with a circular cross-section, a diameter of $1 \mu\text{m}$, or a square with $1 \mu\text{m}$ side. The refractive index of the cylinder $n_1 = 1.4$ ($\varepsilon_1 = 1.96$). The density of the light energy flux is 100 mW/m over the entire diffraction field.

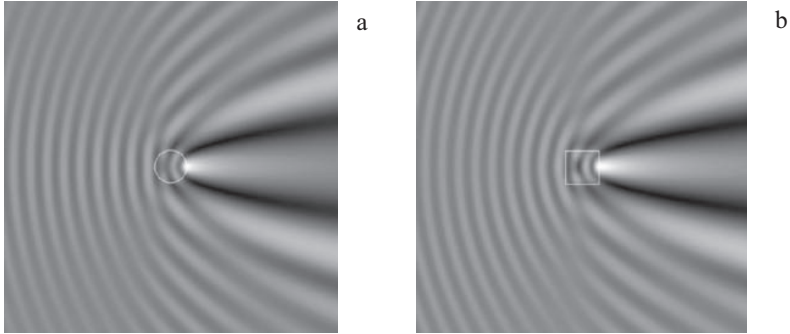


Fig. 8.1. The diffraction field $|E_x|$ of a TE-polarized plane wave on a) a cylinder with a circular cross section and b) a cylinder with a square cross-sectional shape.

Table 8.1. Dependence of the projection of force from the radius of integration

Cylindrical object with a circular cross-section				
$R_i, \mu\text{m}$	5	3.75	2.5	1
$F_z \cdot 10^{-10} \text{ N/m}$	0.33176	0.32036	0.33213	0.31781
Cylindrical object with a square cross-section				
$R_i, \mu\text{m}$	5	3.75	2.5	1
$F_z \cdot 10^{-10} \text{ N/m}$	0.32137	0.31588	0.31792	0.31688

Figure 8.1 shows the amplitude of the diffraction field ($|E_x|$, TE-polarization) of a plane wave on a cylindrical object with the above parameters.

Table 8.1 shows the dependence of the projection of the force F_z acting on the cylinder along the axis of light propagation Z , on the radius of integration R_i . Since the incident wave is flat and extends along the axis Z , the projection of force along the Y axis must be zero. Simulation shows that the projection of force on the Y -axis in this case is three orders of magnitude less than the projection of the force along the axis Z . For example, at the radius of integration $R_i = 5 \mu\text{m}$ for a cylinder with a circular cross-section the projection of force $F_z = 0.33176 \cdot 10^{-10} \text{ N/m}$ and projection $F_y = 0.33176 \cdot 10^{-10} \text{ N/m}$.

As shown in Table 8.1, the fluctuations of the results of calculation of force are less than 5%. The number of samples over the entire diffraction field 256×256 . This result proves that the force is calculated correctly using formulas (8.10) (to within 5%).

Let us consider the dependence of the force, calculated by formulas (8.10), on the resolution of the diffraction field.

Table 8.2. Dependence of the projection of force F_z on the number of counts in the entire diffraction field

$K \times K$	64×64	128×128	256×256	512×512
Cylindrical object with a circular cross-section				
$F_z \cdot 10^{-10}$ N/m	0.4058	0.3523	0.3479	0.3454
Cylindrical object with a square cross-section				
$F_z \cdot 10^{-10}$ N/m	0.3220	0.3259	0.3216	0.3324

Table 8.3. Dependence of the projection of force F_z on the number of samples K taken at the diameter of the circular cylinder

K	12	25	50	100
$F_z \cdot 10^{-10}$ N/m	0.4046	0.3594	0.3497	0.3327

Table 8.2 shows the dependence of the projection of force F_z on the Z axis on the number of counts in the entire diffraction field for the above parameters. The force was calculated for an integration radius of $2.5 \mu\text{m}$. All of the diffraction field was $5 \times 5 \mu\text{m}$ in size.

From Table 8.2 shows that when the number of counts in the entire diffraction field is 64×64 , calculation of the force in the case of a circular cylinder is less accurate due to an error in the description of the boundary of the circular cylinder by a broken line. This does not apply to the last three values of force for a cylinder with a circular cross-section of 2% and 1.5% for the square.

Table 8.3 shows the projection of force F_z in the Z -axis under the same conditions on the number of samples K , taken for the diameter of a cylinder with a circular cross section, at a fixed resolution of the diffraction field – 256×256 pixels.

Table 8.3 shows that at low resolution of the object (in this case 12 samples per diameter of the circular cylinder), the value of the projection of the force acting on the cylinder is considered to be inaccurate. The difference for the last three values of the forces in Table 8.3 is 8%. When taking less than 12 samples per wavelength the iterative algorithm ceases to converge for the given parameters.

8.1.4. Calculation of force for a non-paraxial Gaussian beam

In this section we calculate the projection of force by the formulas (8.10) acting on from the non-paraxial Gaussian beam on a dielectric cylinder with a circular cross section, depending on the displacement L of the centre of the cylinder from the centre of the beam waist.

Projections of the force, calculated by the formula (8.10), acting on a cylinder with a circular cross-section in the case of a TE-polarized wave are shown in Fig. 8.2. The parameters of the experiment: $D = \lambda = 2\omega_0 = 1 \mu\text{m}$, $\varepsilon_2 = 1$ (centre), $\varepsilon_1 = 2$, (object), the power of incident radiation per unit length is $P = 0.1 \text{ W/m}$. The offset from the centre of the waist L has the dimension μm .

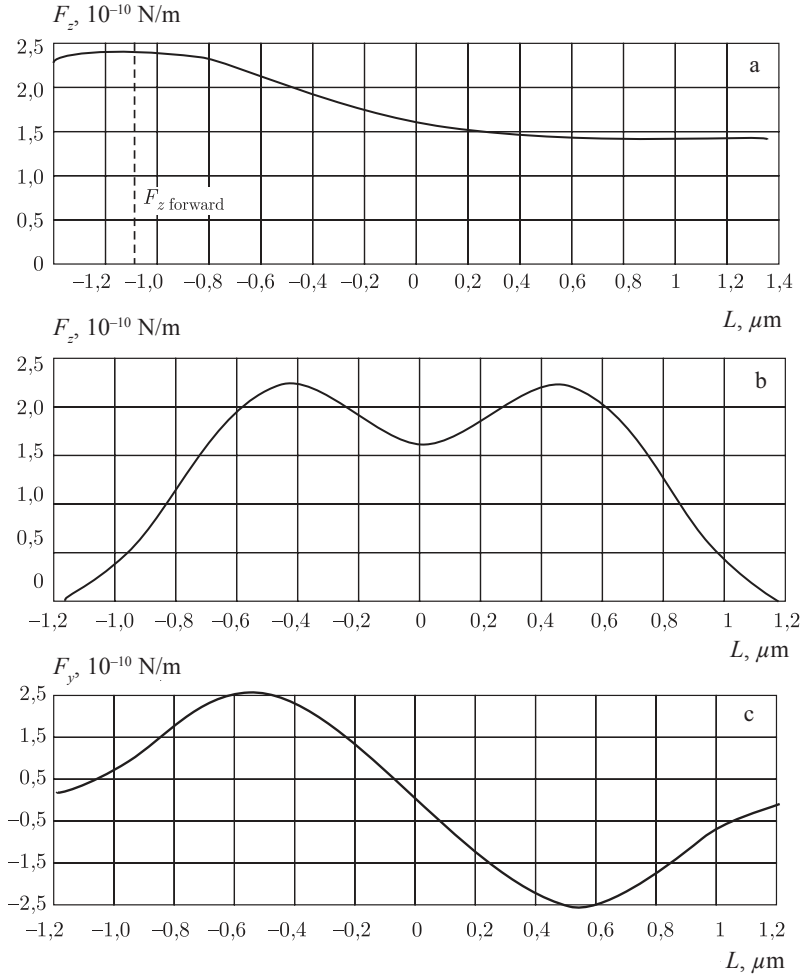


Fig. 8.2. TE polarization: a) the dependence of the projection of force F_z on the displacement L of the object along the Z axis through the centre of the waist ($Y = 0$), b) the dependence of the projections of the forces F_z and F_y on displacement L of the object along the Y axis through the centre of the waist ($Z = 0$).

Similar projections of force in the case of TM-polarization, calculated by the formulas (8.13), are shown in Fig. 8.3.

Figures 8.2b and 8.3b shows that at the transverse displacement of the cylinder along the Y axis there is a projection of force F_y tending to return the cylinder to the centre of the waist. Moreover, the maximum projection of the force F_y and F_z is obtained for the transverse displacement of the cylinder L approximately equal to the radius of the waist of the Gaussian beam: $L \approx \omega_0$.

In [3] the results are presented of numerical simulation of the force acting on a Kerr microsphere in the 3D case. Simulation parameters: the refractive index of the

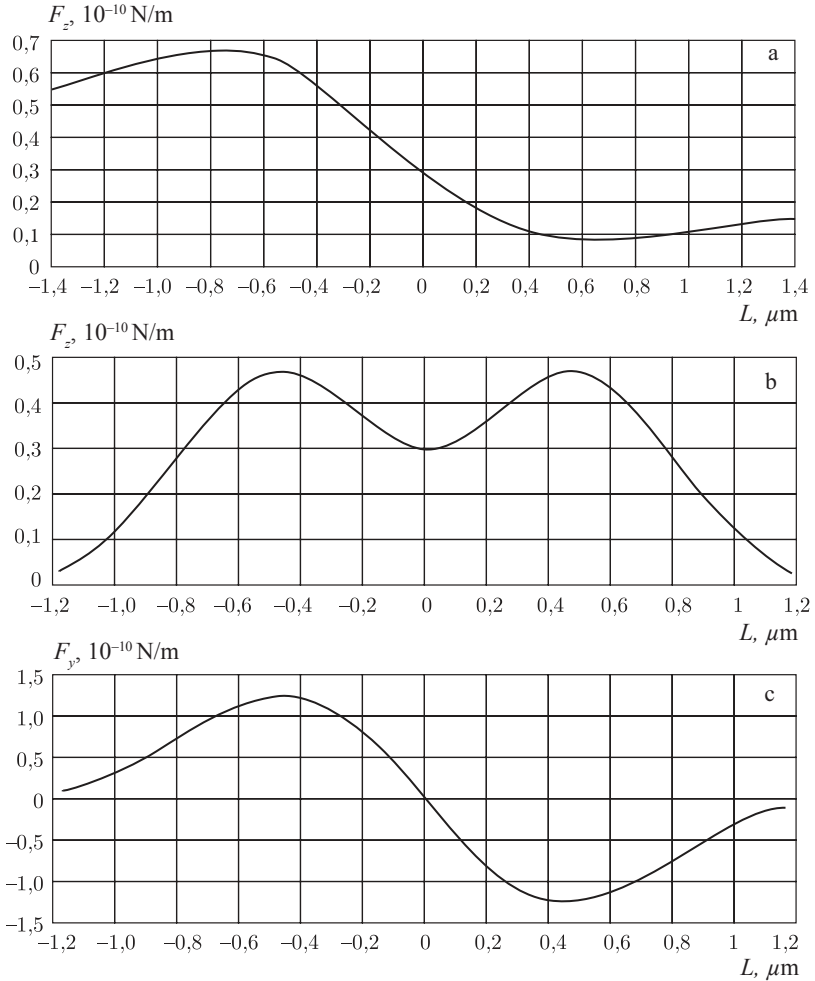


Fig. 8.3. TM-polarization: a) the dependence of the projection of force F_z on the displacement L of the object along the Z axis through the centre of the waist ($Y = 0$), b) the dependence of the projections of the forces F_z and F_y on displacement L of the object along the Y axis through the centre of the waist ($Z = 0$).

sphere $n_1 = 1.4$, refractive index $n_2 = 1.33$, sphere diameter $D = 2 \mu\text{m}$, wavelength $\lambda = 1.06 \mu\text{m}$, relative aperture (the ratio of the aperture of the lens to the focal length) $\text{NA} = 1.4$, the shift from the focus along the axis Z $L = 1 \mu\text{m}$. The force acting perpendicular to the propagation of light when a subject moves from the centre in a plane perpendicular to the propagation of radiation at the given parameters, $F = 0.3 \cdot 10^{-10} \text{ N}$. Figures 8.2b and 8.3b show that the projection of force is of the same order of magnitude per unit length of the cylinder $(0.5\text{--}1) \cdot 10^{-10} \text{ N/m}$.

Figure 8.4 shows the interference pattern of two Gaussian beams directed against each other with a waist at the origin, creating a standing wave. Figure 8.4a shows

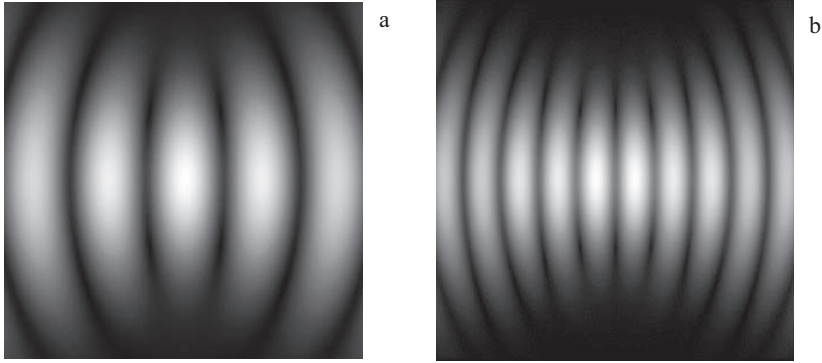


Fig. 8.4. The interference pattern of two non-paraxial Gaussian beams propagating in opposite directions along the axis Z : a) the total amplitude of the electrical field vector $|E_x|$, and b) the projection on the Z axis of the Umov-Poynting vector $|S_z|$.

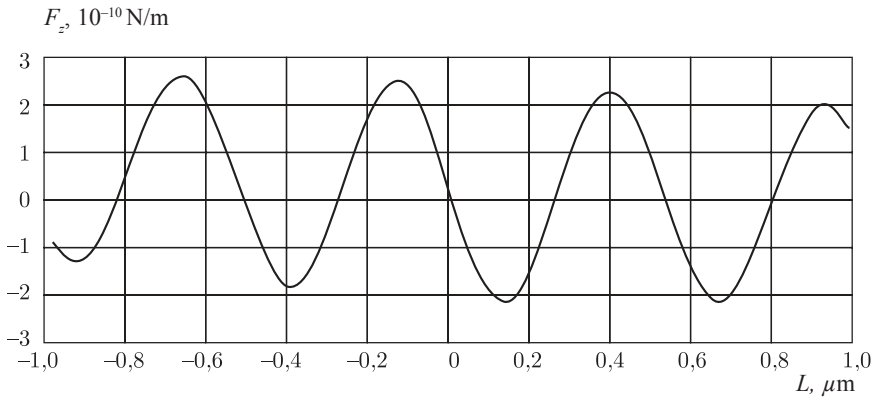


Fig. 8.5. The projection on the Z axis of the force acting on a cylinder with a circular cross section with $\varepsilon_1 = 2$, depending on the displacement of the centre circle of the cylinder along the axis Z .

the amplitude of the total field $|E_x|$ (TE-polarization), Fig. 8.4b is the modulus of the projection of the Umov-Poynting vector on the axis of light propagation Z . The first Gaussian beam is directed along the axis Z , the second beam in the opposite direction of the axis Z . For the first Gaussian beam the wavelength is $1 \mu\text{m}$, the radiation power of 50 mW/m , the Gaussian beam waist is at the origin, its diameter is $1 \mu\text{m}$. The radiation power of the second beam 50 mW/m , the wavelength is also equal to $1 \mu\text{m}$ and the diameter of the waist is $1.5 \mu\text{m}$. If a dielectric object with the size of the order of the wavelength is placed in such a field, then this field will be a trap for him: the object is drawn into the intensity maxima of the field. Figure 8.5 is a plot of the dependence of the projection of force F_z directed along the Z axis on the displacement L from the axis Z . The object is a cylinder with a circular cross section with a diameter of $1 \mu\text{m}$, dielectric constant $\varepsilon_1 = 2$. The diffraction field has a size of $2.5 \times 2.5 \text{ mm}$. Figure 8.5 shows that near the waist along the Z axis almost periodically over a distance of about $0.25 \mu\text{m}$ there are points at which the force is

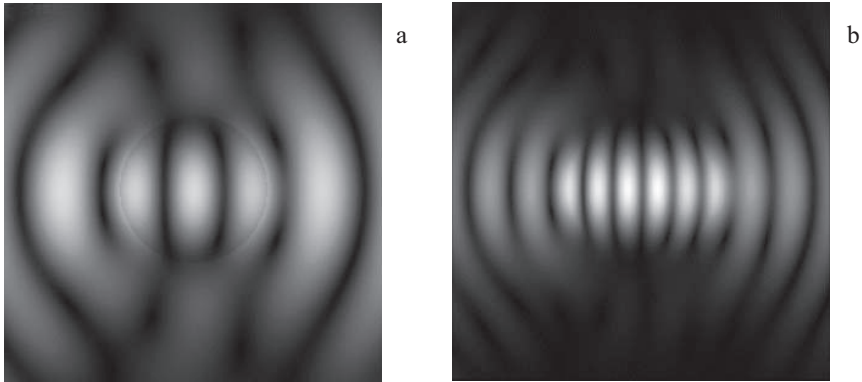


Fig. 8.6 Same as in Fig. 8.4, but in the presence of a cylinder with a circular cross section in the centre of the waist.

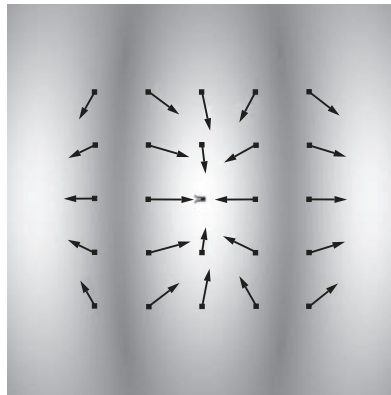


Fig. 8.7 The field vectors of the forces acting on the part of two colliding Gaussian beams on a cylinder with a circular cross section, whose centre is located at different points in the interference pattern: the centre circle of the cylinder coincides with the beginning of each hand, and the length of each arrow is proportional to the modulus of strength at this point.

zero. If the centre of the cylinder coincides with these points, then the cylinder will be in a stable or unstable equilibrium. The points of stable and unstable equilibria alternate, that is, approximately every $0.5 \mu\text{m}$ the cylinder will be in the ‘optical trap’ (at the point of stable equilibrium).

Figure 8.6 shows the diffraction of Gaussian beams directed against each other, shown in Fig. 8.4, on a cylinder with a circular cross section, as described above. Figure 8.6a represents the strength of the electric field $|E_x|$ (TE-polarization), Fig. 8.6b – a projection of the Umov–Poynting vector on the axis Z . The object is located in the centre of the waist ($z = 0$). For visualization, the object in Fig. 8.6a is slightly obscured itself.

Figure 8.7 shows the central part of the diffraction pattern in Fig. 8.6a with the size of $0.31 \times 0.31 \mu\text{m}$. The arrows displayed the direction of the force acting on this

cylinder by radiation, with the object placed in each specific point in space. One can see that the object is ‘drawn’ into the maxima of the interference pattern. The length of the arrows is proportional to absolute force.

If the refractive index is less than the refractive index of the particles, under certain conditions one can observe the ‘capture’ of the particle along the Z axis, not only in the case of two colliding beams, but also in the case of a focused Gaussian beam.

Figure 8.8 shows a graph of the projection of force F_z in the displacement of the cylinder over distance L along the axis Z. The parameters of the experiment: the wavelength $1 \mu\text{m}$, the diameter of the Gaussian beam waist $2\omega_0 = 1 \mu\text{m}$, the dielectric constant of the particles $\epsilon_1 = 1.2$, the medium $\epsilon_2 = 1$, the particle diameter $D = 2 \mu\text{m}$. From the graph we can see the capture mechanism: the projection of force F_z in front of the focus is positive and directed towards the focus, behind the focus it is negative and pushes the particle back into focus. From numerical experiments it was determined that the ability to capture depends on the dielectric constant of the particle. For the given parameters ‘capture’ occurs when $1 < \epsilon_1 < 1.35$. A plot of the force F_z under these parameters and the dielectric constant of the particle $\epsilon_1 = 1.35$ is shown in Fig. 8.8.

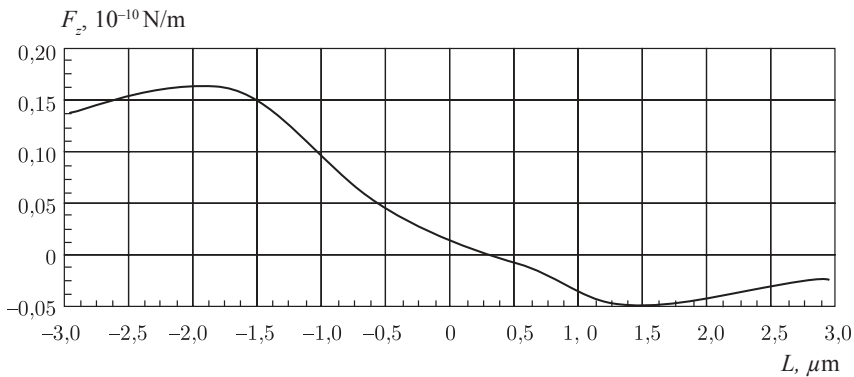


Fig. 8.8 The projection of force in the Z axis for a Gaussian beam acting on a cylinder with a circular cross section with $a = 1.2$ (medium = 1).

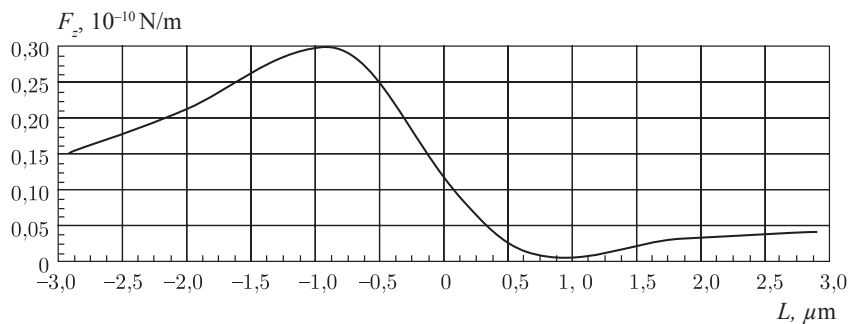


Fig. 8.9. The boundary of ‘capture’: the projection of force in the Z axis for a nonparaxial Gaussian beam and a cylinder with a circular cross section with $a = 1.35$.

Figure 8.8 shows that in the displacement of the cylinder along the optical axis at a distance $L \approx 0.4 \mu\text{m}$ the force exerted on it by the light beam goes to zero: $F_y = F_x = 0$. The existence of such an equilibrium point for the cylinder can be explained in terms of the two forces (scattering and gradient) acting on the cylinder near the waist of the Gaussian beam. Indeed, when the centre of the cylinder is exactly in the centre of the beam waist, then it is subjected only to the scattering force (photons push the cylinder forward), which is proportional to the intensity $|E_x|^2$. At the offset from the centre of the cylinder along the optical axis a gradient force arises due to the presence of the gradient of intensity $\Delta|E_x|^2$, which is aimed at the centre of the beam. At displacement $L \approx 0.4 \mu\text{m}$ those forces are compared and the cylinder is in equilibrium.

A real cylindrical object has a finite length. But the two-dimensional approximation, which we consider here, can be applied to the description of the real situation if the length of the cylinder will be much larger than the diameter of its cross section. Indeed, consider the case where a three-dimensional dielectric cylinder of finite length is located near the waist of a cylindrical Gaussian beam (see Fig. 8.10).

Let the cylinder axis tilted at an angle θ , in the plane XY . Then the maximum deviation from the stable equilibrium point of the cylinder cross-section in the YZ plane will be equal to $\Delta y = l \cdot \text{tg}(\theta)$, $y/a \ll 1$, where l is the length of the cylinder, a is the radius of its cross section. This results in a projection force F_y , directed to the point of maximum intensity on the beam axis. That is, small rotations and displacements of the three-dimensional finite-length cylinder near a stable equilibrium of the cylindrical Gaussian beam waist will give rise to forces seeking to return the cylinder to the ‘optical trapping’ position.

8.1.5 Calculation of forces for the refractive index of the object smaller less than the refractive index of the medium

It is interesting to calculate the light force and field, acting on a dielectric 2D object whose refractive index is smaller than that of the medium.

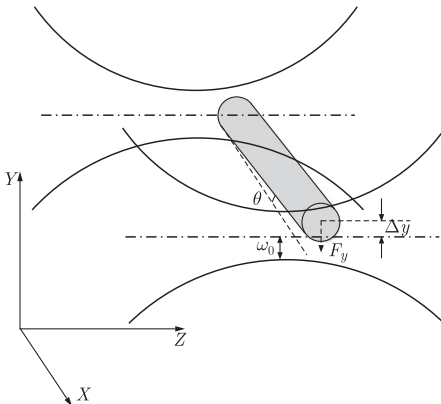


Fig. 8.10. Reflection of the slope of a three-dimensional finite cylinder in the two-dimensional model.

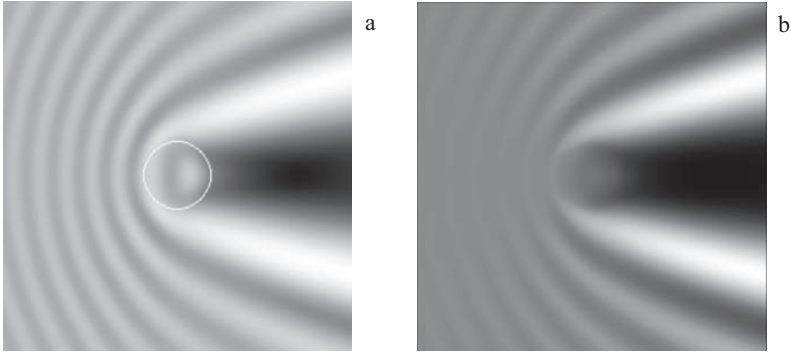


Fig. 8.11. Modulus of the strength of the electric field $|E_x|$ (a) and modulus of the projection of the Umov–Poynting vector on the axis Z $|S_z|$ (b) for diffraction of a plane wave on an air cylinder with a circular cross section in water.

Figure 8.11 shows the diffraction pattern of a plane wave in a medium with a refractive index $n_2 = 1.33$ (water) on a cylindrical object with a circular cross section with a refractive index $n_1 = 1$ (cylindrical air bubble). The diameter of the cylinder is equal to the wavelength and is equal to $1 \mu\text{m}$. Figure 8.11a is the modulus of the strength of the electric field $|E_x|$ (TE-polarization), Fig. 8.11b is a projection of the Umov–Poynting vector on the axis Z . The energy does not propagate behind the ‘air bubble’ which can be clearly seen on the sections shown in Fig. 8.12, taken along the Z axis through the point $Y = 0$.

Figure 8.12a shows the value of the amplitude $|E_x|$, Fig. 8.12b – the projection of the Umov–Poynting vector on the axis Z .

If such an object is placed near the focus of a Gaussian beam, it will be pushed out of it, as illustrated in the graphs in Fig. 8.13.

Figure 8.13a is a plot of the dependence of the force F_z along the Z axis on the displacement L along the axis Z , Fig. 8.13b – the dependence of force F_y on the displacement L along the Y axis through the focus. The Gaussian beam has a wavelength of $1 \mu\text{m}$, the diameter of the waist is $1 \mu\text{m}$, the radiation power 100 mW/m . It is seen that in deviation in either direction from the focus in the transverse direction the force, directed toward the deflection, increases, which leads to the movement of the focus in this direction. In deviation along the axis Z of light the force exerted on an object in front of the focus is less in the absolute value than behind the focus.

8.2 Methods for calculating the moment of force acting on a micro-object by a focused laser beam

In this section, we calculate the moment of force acting on a cylindrical micro-object with an elliptical cross-section from the side of the focused non-paraxial Gaussian beam. Calculation of the moment of the force was conducted depending on the size and shape of the integration region encompassing the micro-object under

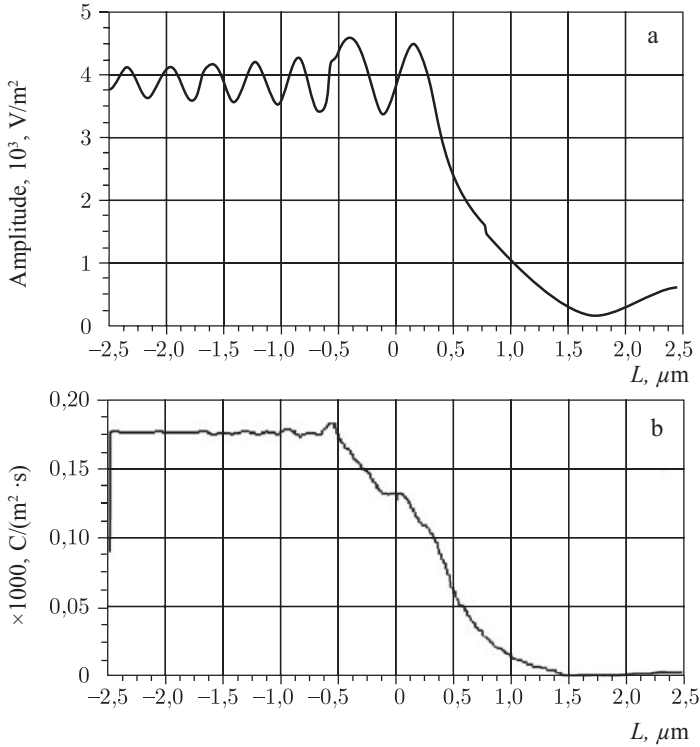


Fig. 8.12. Section of Fig. 8.11a (a) and 8.11b (b) along the Z axis through the point $Y = 0$.

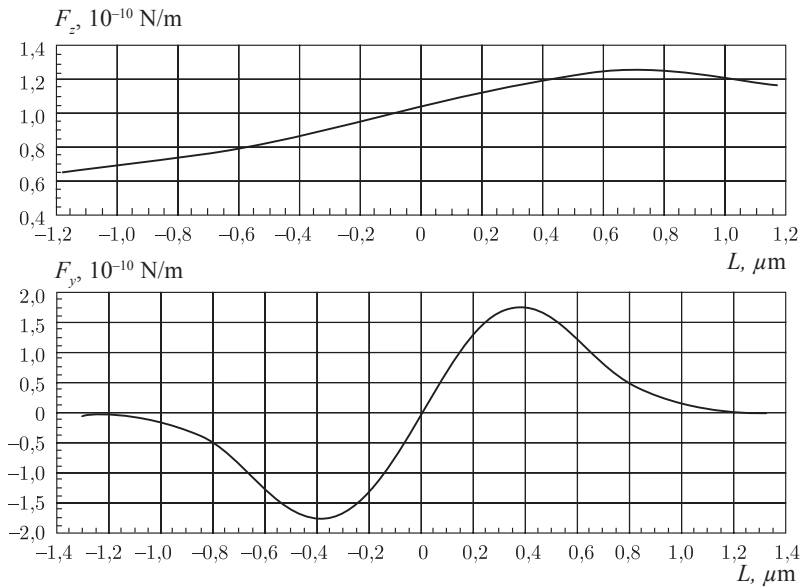


Fig. 8.13. The projections of the force of the non-paraxial Gaussian beam on 'a cylindrical air bubble' in the water: on the longitudinal axis F_z (a) and transverse axis F_y (b).

study. We consider the the moment of the force on the micro-object, located at the point where the force exerted by light is zero. We also consider a moment of force acting on the micro-object with an elliptical section in the standing wave.

8.2.1. The orbital angular momentum in cylindrical microparticles

Figure 8.14 shows the scheme of the problem.

Light propagates along the Z axis in a medium with permittivity ε_1 and falls on an object with a dielectric constant ε_2 . Then the moment \mathbf{M} at any point A can be calculated using the formula [4]:

$$\mathbf{M} = \oint_S \left[\mathbf{r} \times (\tilde{\mathbf{T}} \cdot \mathbf{n}) \right] dS, \quad (8.14)$$

where \mathbf{n} is the normal to the surface S , covering the object in question, A is the point at which we calculated moment \mathbf{M} , \mathbf{r} is the radius vector from point A to the integration surface S , $\tilde{\mathbf{T}}$ is the Maxwell's stress tensor of the electromagnetic field.

The product of the Maxwell stress tensor on the normal can be written as:

$$\begin{aligned} (\tilde{\mathbf{T}} \cdot \mathbf{n}) &= \begin{bmatrix} T_{ii} & T_{ij} & T_{ik} \\ T_{ji} & T_{jj} & T_{jk} \\ T_{ki} & T_{kj} & T_{kk} \end{bmatrix} \begin{pmatrix} n_x \\ n_y \\ n_z \end{pmatrix} = \\ &= \begin{bmatrix} T_{ii}n_x + T_{ij}n_y + T_{ik}n_z \\ T_{ji}n_x + T_{jj}n_y + T_{jk}n_z \\ T_{ki}n_x + T_{kj}n_y + T_{kk}n_z \end{bmatrix} = \begin{pmatrix} t_x \\ t_y \\ t_z \end{pmatrix}. \end{aligned} \quad (8.15)$$

Then

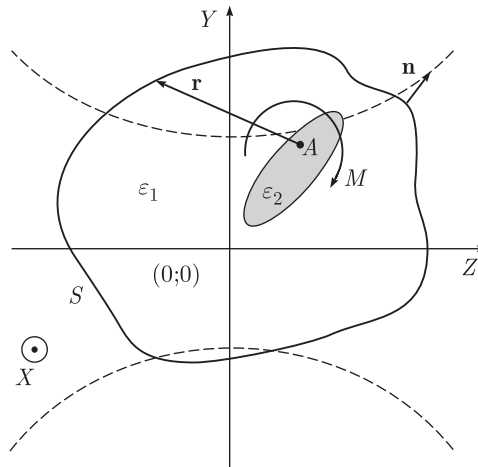


Fig. 8.14. Scheme of the problem.

$$\mathbf{r} \times (\tilde{\mathbf{T}} \cdot \mathbf{n}) = \begin{bmatrix} i & j & k \\ r_x & r_y & r_z \\ t_x & t_y & t_z \end{bmatrix} = \mathbf{i}(r_y t_z - r_z t_y) - \mathbf{j}(r_x t_z - r_z t_x) + \mathbf{k}(r_x t_y - r_y t_x). \quad (8.16)$$

For the two-dimensional case (cylindrical object) this makes sense only in relation to the axis X , i.e.

$$M_x = \oint_S (r_y t_z - r_z t_y) dS. \quad (8.17)$$

As $E_y = E_z = H_x = 0$, for TE-polarization, we finally obtain:

$$\begin{aligned} M_x &= \frac{1}{4} \oint_S \left[\varepsilon_0 \varepsilon_1 |E_x|^2 + \mu \mu_0 |H_y|^2 - \mu \mu_0 |H_z|^2 \right] \times \\ &\times r_y dy - \frac{1}{2} \oint_S \mu \mu_0 \operatorname{Re} (H_z H_y^*) r_y dz - \\ &- \frac{1}{4} \oint_S \left[\varepsilon_0 \varepsilon_1 |E_x|^2 - \mu \mu_0 |H_y|^2 + \mu \mu_0 |H_z|^2 \right] r_z dz - \\ &- \frac{1}{2} \oint_S \mu \mu_0 \operatorname{Re} (H_y H_z^*) r_z dy. \end{aligned} \quad (8.18)$$

Calculation of the final formula for the moment for TM-polarization differs by the substitution in (8.17) $E_x = H_y = H_z = 0$.

8.2.2. The results of numerical simulation of the force moment

To verify the correctness of the formula (8.18), we calculated the moment of force acting on a elliptical microparticle by a non-paraxial Gaussian beam with different sizes of square integration contour S . Figure 8.15b shows a plot of the changes of moment M_x in the integration contour, whose parameters are shown in Fig. 8.15a. The waist of the Gaussian beam is located in the centre of coordinates, the light propagates in the positive direction along the axis Z .

The diffraction field is calculated by the method described in the previous section. The integration was carried out on the square contour S , the number of counts in Fig. 8.15a 254×254. This is convenient because it is not necessary to calculate the normal \mathbf{n} at each point of the circuit – the contour integral (8.18) splits into a sum of integrals, some of which are taken on the contour sides parallel to the axis Y , and another part on the sides of the contour parallel to the axis Z . The power of the incident radiation was equal to $P = 100$ mW/m, the wavelength $\lambda = 1$ μm, the dielectric constant of the medium $\varepsilon_1 = 1$, the dielectric constant of the particle $\varepsilon_2 = 2$. Point A , in relation to which the moment is calculated, coincides with the centre of an elliptical particle.

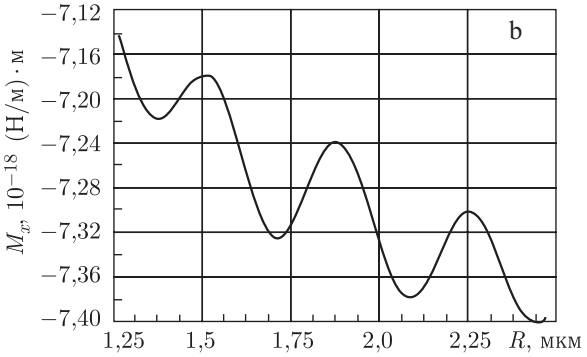
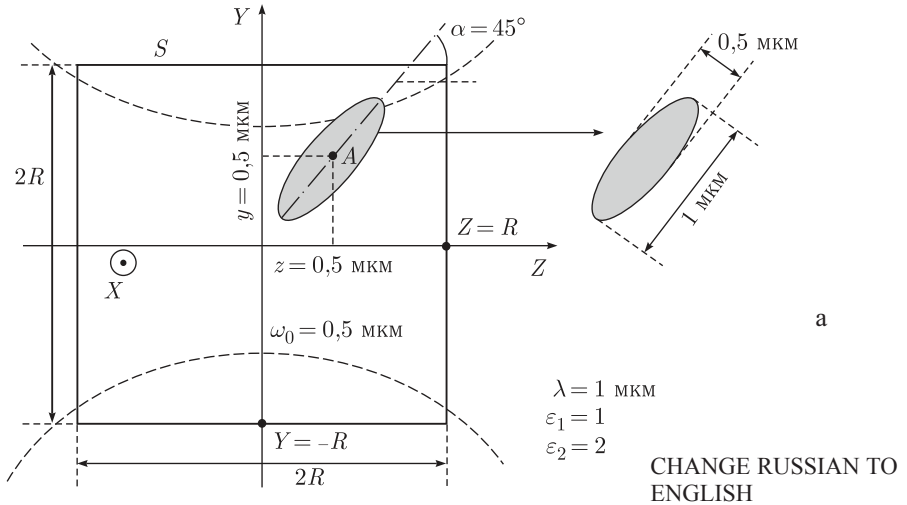


Fig. 8.15. a) The calculation of the moment of force and b) the results of the calculation of moment M_x for different R .

Note that the moment of force \mathbf{M} is measured in units $[\text{N} \cdot \text{m}]$. However, in this case the dimension of M_x is $[(\text{N} \cdot \text{m}) \cdot \text{m}]$ because the force in the two dimensional case is expressed, due to an infinitely long cylindrical object along the X axis, in units N/m and is unit force per unit length of the micro-object.

Figure 8.15b shows that the fluctuations in the value of M_x with a change in R are less than 4%.

Note that the magnitude of the moment of force \mathbf{M} depends on the location of point A , relative to which it is calculated, if the force acting on the particle is not zero. If we calculate the moment of force M_x for the scheme in Fig. 8.15a at the same location of the cylinder, but when the point A has coordinates $(0.25 \mu\text{m}, 0.25 \mu\text{m})$, the value will be $M_x = 8.8 \cdot 10^{-17} (\text{N} \cdot \text{m}) \cdot \text{m}$.

Figure 8.16 shows the scheme of calculating the moment of the force M_x for the case when the force of light acting on a particle is zero. An elliptical cylinder with dielectric constant $\epsilon_2 = 2$ is in the water with $\epsilon_1 = 1.77$.

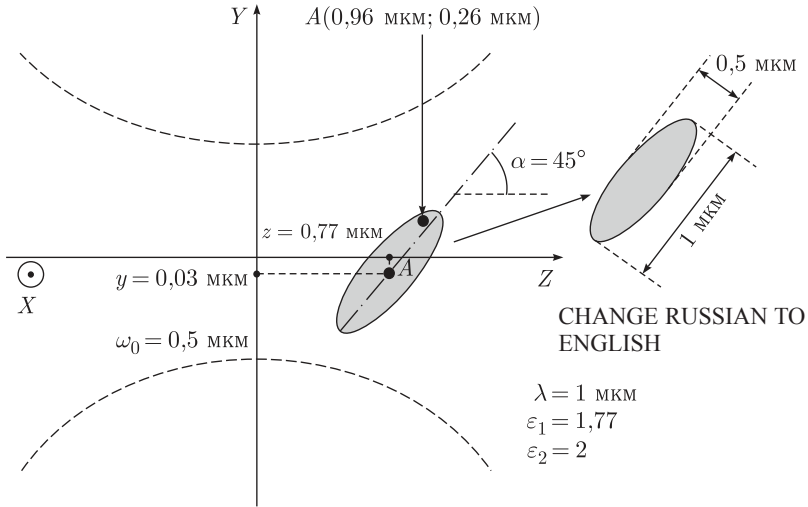


Fig. 8.16. Calculation of the moment of force in finding the elliptical cylinder at the equilibrium point (the force of the light to an object is equal to zero)

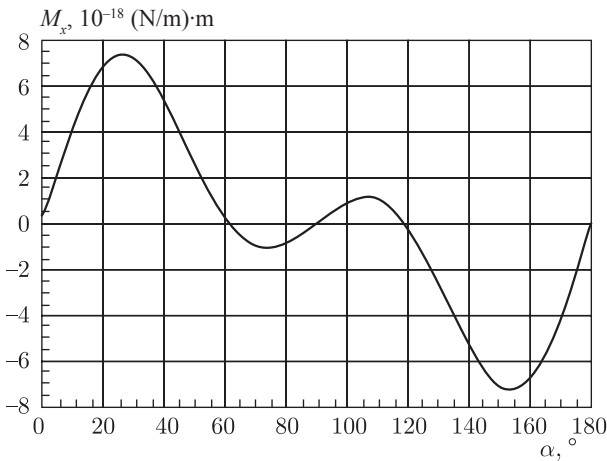


Fig. 8.17. Dependence of the projection on the X axis of the moment of force acting on the elliptical cylinder in the focus of a Gaussian beam, on angle α .

The moment of force in finding the elliptical cylinder at the focus with point A , located in the centre of the particle, is $M_x = 7.11 \cdot 10^{-8} \text{ (N/m)·m}$. If we move the observation point A to a point with the coordinates $(0.96 \mu\text{m}, 0.26 \mu\text{m})$, then the moment will be equal to $M_x = 7.11 \cdot 10^{-8} \text{ (N/m)·m}$. Thus, we see that the moment of force acting on the particle is almost independent of the point relative to which it is calculated, if the particle is at the point where the force exerted by the light field is zero.

Figure 8.17 shows a plot of the dependence of the moment of force on angle α . The simulation parameters are the same as in Fig. 8.15a, but the object is located

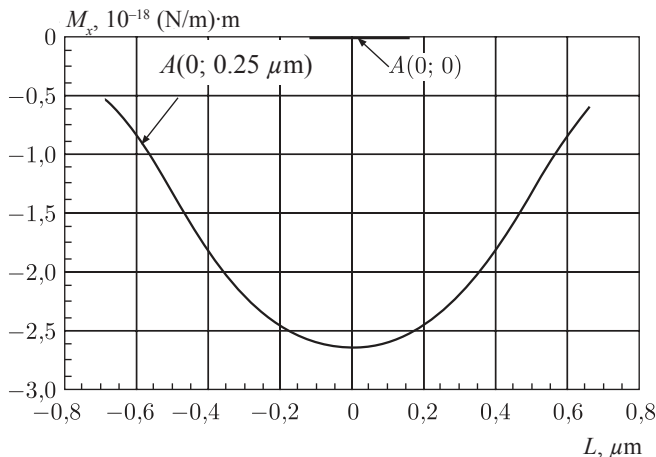


Fig. 8.18. The dependence of the moment M_x on the displacement L of a spherical particles along the Y axis for the two positions of point A relative to the centre of the particle.

in the centre of the waist, point A is located in the centre of the object, the major diameter of the ellipse is $1.2 \mu\text{m}$, minor $0.3 \mu\text{m}$, the dielectric constant of the object $\varepsilon_1 = 2.25$. The angle α was determined as shown in Figure 8.16 (measured from the Z -axis counter-clockwise).

Figure 8.17 shows that the positions of the elliptical particle in the focus when its long axis lies along and perpendicular to the optical axis, are stable equilibria ($M_x > 0$ for a particle rotating in the clockwise direction). When α is approximately equal to 60° and 120° , there are two points of unstable equilibrium, when the moment vanishes. This agrees well with the data in [4], where the same plot of the dependence the moment of force on the rotation angle of the particle α was obtained

Figure 8.18 is a plot of the dependence of the moment of force M_x on the displacement L of a circular particle with a radius of $0.25 \mu\text{m}$ on the Y axis through the centre of the waist. Point A is located in the centre of particle $A(0, 0)$ and $0.25 \mu\text{m}$ above the centre of the Y axis. The other parameters are the same as in Fig. 8.15.

As can be seen from Fig. 8.18 the moment of force acting on a circular non-absorbing particle in relation to the centre is equal to zero when it is displaced along the Y axis, and varies with the displacement of point A up by $0.25 \mu\text{m}$ from the centre of the particle along the Y axis. If to the function, describing the dielectric permittivity of the particles, we add an imaginary component (the absorbing particle), the moment of force on the circular particle in relation to the centre will be different from zero at the displacement of the particle identical to that in Fig. 8.18. Figure 8.19 shows a plot of the dependence of the moment of force acting on a circular particle with $\varepsilon_2 = 2 + 1i$ with respect to the centre of the particle. The other parameters are the same as in the calculation of the graph in Fig. 8.18.

As can be seen from Fig. 8.19, the moment of force acting on a circular absorbing particles relative to the centre is not equal to zero when the particle is displaced from the optical axis.

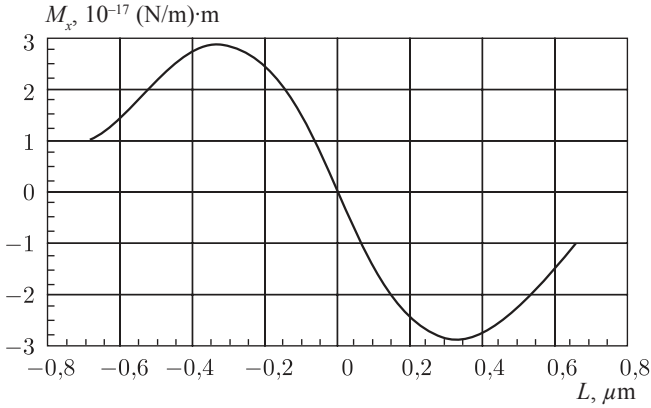


Fig. 8.19. The dependence of the moment of force on a circular displacement L of the absorbing particles (ϵ_2) along the Y axis with respect to point $A(0, 0)$

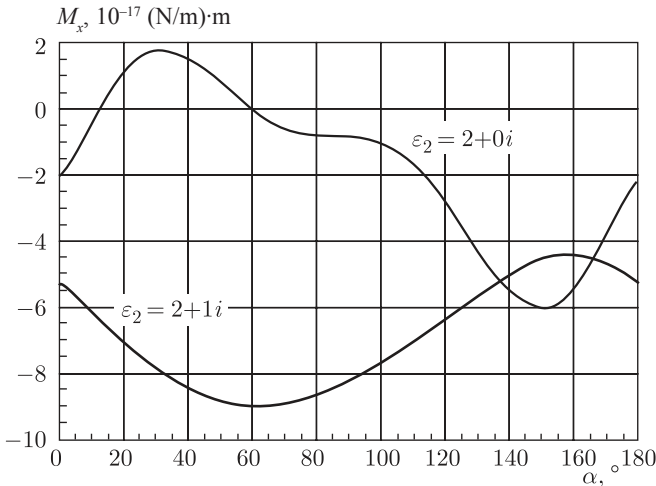


Fig. 8.20. The dependence of the moment of force M_x on the elliptical particle on the rotation angle α of the particle.

Figure 8.20 is a plot of the dependence of the moment of force M_x acting on an elliptical dielectric ($\epsilon_2 = 2 + 0i$) and absorbing microparticles ($\epsilon_2 = 2 + 0i$), on the angle of rotation of the particle α . The particle is located in the coordinates $(0, 0.25)$ with respect to the beam waist, the moment was calculated relative to the centre of the ellipse. The other simulation parameters are the same as in Fig. 8.15a.

As can be seen from Fig. 8.20, the addition of the imaginary part to the function of dielectric permittivity of the particle increases the scattering strength, due to which at any angle α the moment of force is non-zero and is directed counterclockwise ($M_x < 0$).

Figure 8.21a shows the results of the calculation of the dependence of the moment M_x acting on the elliptical particle, located at the centre of the Gaussian beam, on the

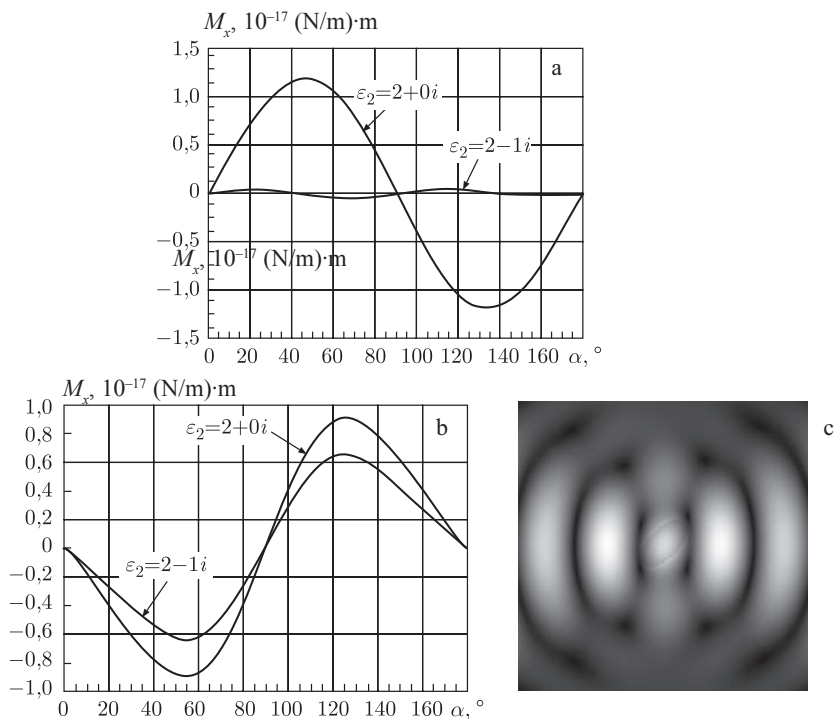


Fig. 8.21. a) The dependence of the moment M_x on the angle α for a single Gaussian beam b) the dependence of moment M_x on angle α for the two oppositely directed Gaussian beams, c) the amplitude of the field $|E_x|$ of two oppositely directed Gaussian beams on an elliptical particle.

angle of rotation α . All parameters are the same as in Figure 8.15a, the particle is taken only half the size (the smaller diameter of the ellipse $0.25 \mu\text{m}$, larger diameter $0.5 \mu\text{m}$), the dielectric constant and the particle is taken. Figure 8.21b shows the same chart, but for the two Gaussian beams, the first waist radius $\sigma_1 = 0.5 \mu\text{m}$, second $\sigma_2 = 0.6 \mu\text{m}$, the intensity of the two Gaussian beams was the same and equal to 50 mW/m^2 . Diffraction of the oppositely directed beams of on a particle at $\alpha = 45^\circ$ is shown in Fig. 8.21c.

As can be seen from Fig. 8.21, by adding the imaginary part of dielectric permittivity if the cylinder is located in the centre of the waist of a Gaussian beam, the moment of force is strongly attenuated and has several zero points. It is also clear that the position of stable equilibrium when adding a second oppositely directed Gaussian beam will be observed at the location of the major axis of an elliptical particle along the axis Y , i.e. the elliptical particle tends to settle along the line of maximum intensity.

8.3. A geometrical optics method for calculating the force acting by light on a microscopic object

8.3.1. Description of the method

As can be seen in the previous section in the problem of calculating the electromagnetic forces in the approach is very capacious as regards the volume of calculations, as well as in the problems of calculating the forces acting on the micro-object in the light beam it is generally required to calculate the forces in some areas; consequently, the amount of computation grows as the square of the size of the area. In this case, for example, the calculation of forces to simulate the motion of the micro-object can take dozens of hours on a PC. In this regard, we use a simple geometrical optics approach, which gives approximate results. The geometrical optics approach has been used in the calculation of the simplest optical traps [32]. However, this and other studies generally considered some of the simpler cases in which restrictions are imposed either on the form of the micro-object [32, 86], or the shape of the beam [78]. We consider the method of calculating the forces acting on the micro-object of arbitrary shape in a light beam with a given distribution of intensity and phase [15].

Consider the micro-object of arbitrary shape in the light beam. We assume that the observed number of conditions:

1. The light beam is given by functions of intensity $I(x, y)$ and phase $\varphi(x, y)$.
2. The micro-object is bounded by two surfaces: the top, which is given by the function $f_1(x, y)$ and the bottom, which is given by the function $f_2(x, y)$ (Fig. 8.22). The functions $f_1(x, y)$ and $f_2(x, y)$ are unique.
3. Micro-object is moving in the plane xy (however, this method is easy to calculate the force extends to three-dimensional motion).
4. The light beam is incident on the micro-object vertically from top to bottom.

Unit vectors $\vec{\mathbf{a}}(a_x, a_y, a_z)$, $\vec{\mathbf{b}}(b_x, b_y, b_z)$, $\vec{\mathbf{c}}(c_x, c_y, c_z)$ define the direction of the incident and refracted rays. The vector $\vec{\mathbf{a}}(a_x, a_y, a_z)$ is determined by the function $\varphi(x, y)$. This vector must always be perpendicular to the wavefront.

The components of the force \mathbf{F} of a single beam on the micro-object are determined by the formula

$$\begin{aligned} F_x &= \frac{N}{c}(a_x - c_x), \\ F_y &= \frac{N}{c}(a_y - c_y), \end{aligned} \tag{8.19}$$

where N is the power of the beam, c is the velocity of light.

For the whole beam, this formula takes the form

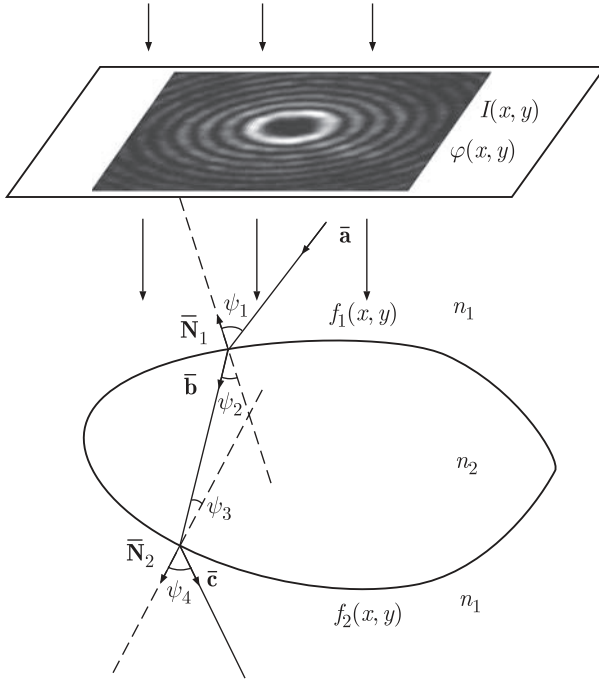


Fig. 8.22. Scheme of refraction of light rays on a micro-object.

$$F_x = \frac{1}{c} \iint_{\Omega} I(x, y) (a_x - c_x) dx dy, \quad (8.20)$$

$$F_y = \frac{1}{c} \iint_{\Omega} I(x, y) (a_y - c_y) dx dy,$$

where Ω is the region of maximum cross-sectional area of a microscopic object in a plane perpendicular to the direction of propagation of the light beam.

It should be borne in mind that the direction vector for the refracted output beam depends on the direction vector of the incident beam

$$F_x = \frac{1}{c} \iint_{\Omega} I(x, y) (a_x - c_x(\bar{\mathbf{a}})) dx dy, \quad (8.21)$$

$$F_y = \frac{1}{c} \iint_{\Omega} I(x, y) (a_y - c_y(\bar{\mathbf{a}})) dx dy.$$

The dependence $\bar{\mathbf{c}}(\bar{\mathbf{a}})$, i.e. direction of the beam after the micro-object, depending on the initial beam direction, can be determined from the following relations

$$\begin{aligned}
(\vec{\bar{N}}_1, -\vec{\bar{a}}) &= \cos(\psi_1), \\
(\vec{\bar{N}}_1, -\vec{\bar{b}}) &= \cos(\psi_2), \\
(\vec{\bar{a}}, \vec{\bar{b}}) &= \cos(\psi - \psi_{21}), \\
n_1 \sin \psi_1 &= n_2 \sin \psi_2, \\
(\vec{\bar{N}}_2, \vec{\bar{b}}) &= \cos(\psi_3), \\
(\vec{\bar{N}}_2, \vec{\bar{c}}) &= \cos(\psi_4), \\
(\vec{\bar{b}}, \vec{\bar{c}}) &= \cos(\psi_3 - \psi_4), \\
n_2 \sin \psi_3 &= n_1 \sin \psi_4,
\end{aligned} \tag{8.22}$$

where n_1, n_2 are the refractive indices of the medium and micro-object, $\vec{\bar{N}}_1$ and $\vec{\bar{N}}_2$ are the normal vectors to the surfaces $f_1(x, y)$ and $f_2(x, y)$, $\psi_1, \psi_2, \psi_3, \psi_4$ are the angles of incidence and refraction at the surfaces. By simple transformations we obtain from (8.22)

$$b_x = \frac{A_1^2}{A_1^2 + A_2^2} \left[\left(\frac{A_3 A_2}{A_1} + K_1 K_2 \right) + \sqrt{\left(\frac{A_3 A_2}{A_1^2} + K_1 K_2 \right)^2 - \left(1 + \frac{A_2^2}{A_1^2} + K_1^2 \right) \left(\frac{A_3^2}{A_1^2} + K_1^2 - 1 \right)} \right]. \tag{8.23}$$

Here we have introduced a number of intermediate symbols which can significantly simplify the writing of the formula:

$$\begin{aligned}
A_1 &= a_y - \frac{N_{1y} a_z}{N_{1z}}, & A_2 &= a_x - \frac{N_{1x} a_z}{N_{1z}}, \\
A_3 &= \frac{a_z \cos \psi_2}{N_{1z}} + \cos(\psi_1 + \psi_2), \\
K_1 &= \frac{\cos \psi_2}{N_{1z}} - \frac{N_{1y} A_3}{A_1}, & K_2 &= \frac{N_{1x}}{N_{1z}} - \frac{N_{1y} A_2}{A_1}.
\end{aligned}$$

The same calculation procedure is used to determine other components of the vectors $\vec{\bar{b}}(b_x, b_y, b_z)$ and $\vec{\bar{c}}(c_x, c_y, c_z)$. Since the cumulative record of these formulas is very large and is similar to the formula (8.23), it will not be presented here.

To determine the components of the direction vector $\vec{\bar{a}}(a_x, a_y, a_z)$ we need to use the phase $\varphi(x, y)$ of the light beam. As mentioned above, the direction vector must always be perpendicular to the wavefront. Then the direction vector is described by the following relation

$$\bar{\mathbf{a}} = \frac{\text{grad}\phi(x,y)}{|\text{grad}\phi(x,y)|}. \quad (8.24)$$

For normal vectors we can write the relation

$$\begin{aligned} \bar{\mathbf{N}}_1 &= \left(\frac{\frac{\partial f_1}{\partial x}}{\sqrt{\left(\frac{\partial f_1}{\partial x}\right)^2 + \left(\frac{\partial f_1}{\partial y}\right)^2 + 1}}, \frac{\frac{\partial f_1}{\partial y}}{\sqrt{\left(\frac{\partial f_1}{\partial x}\right)^2 + \left(\frac{\partial f_1}{\partial y}\right)^2 + 1}}, -\frac{1}{\sqrt{\left(\frac{\partial f_1}{\partial x}\right)^2 + \left(\frac{\partial f_1}{\partial y}\right)^2 + 1}} \right), \\ \bar{\mathbf{N}}_2 &= \left(\frac{\frac{\partial f_2}{\partial x}}{\sqrt{\left(\frac{\partial f_2}{\partial x}\right)^2 + \left(\frac{\partial f_2}{\partial y}\right)^2 + 1}}, \frac{\frac{\partial f_2}{\partial y}}{\sqrt{\left(\frac{\partial f_2}{\partial x}\right)^2 + \left(\frac{\partial f_2}{\partial y}\right)^2 + 1}}, -\frac{1}{\sqrt{\left(\frac{\partial f_2}{\partial x}\right)^2 + \left(\frac{\partial f_2}{\partial y}\right)^2 + 1}} \right). \end{aligned} \quad (8.25)$$

Similarly, we determine the parameters of the reflected light rays (Fresnel reflection). Using (8.21)–(8.25), we can calculate the force acting on an arbitrarily shaped micro-object from an arbitrary light beam. Knowing the mechanical properties of the medium in which the micro-object is located, we can also simulate the motion of a microscopic object. In modeling the motion of a microscopic object in the light beam was solved by a system of equations of motion.

$$\begin{cases} m \frac{d\mathbf{v}}{dt} = \mathbf{F}_l + \mathbf{F}_f, \\ \frac{d\mathbf{r}}{dt} = \mathbf{v}, \end{cases}$$

where \mathbf{F}_l is the force acting on the micro-object from the light beam, \mathbf{F}_f is the force of viscous friction. Based on the above proposed method software has been developed that allows one not only to calculate the force of the light on the microscopic object in a given light field, but also to simulate the motion of a microscopic object in a given environment. Figure 8.23 shows the interface of the software.

However, the geometrical optics approach for the micro-objects comparable in size to the wavelength usually gives very inaccurate results where we need to calculate, for example, the intensity behind a microscopic object. It is necessary to verify how we apply this approach to calculate the force of light. To do this, we compare the values of force obtained by two methods: geometrical optics, which has been described in this section, and the electromagnetic method, which was described in Section 8.1.

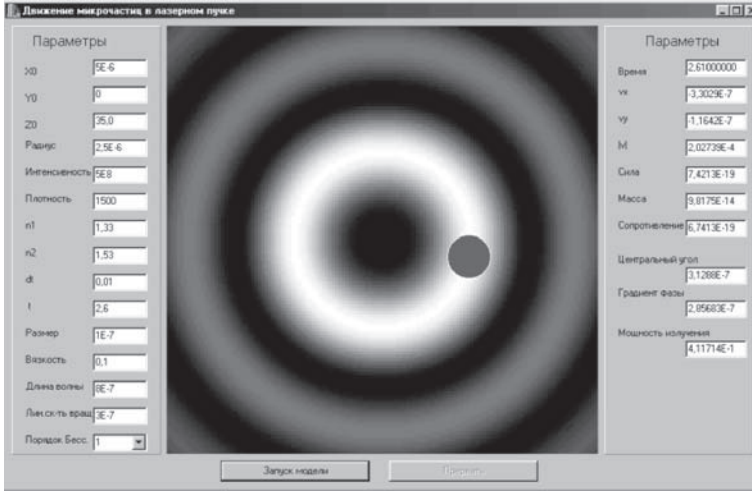


Fig. 8.23. Interface software for the simulation of the motion of microscopic objects in the light field.

8.3.2. Comparison of results of calculations by geometrical optics and electromagnetic methods

The method of calculating the force (8.19)–(8.25) allows us to calculate the effect of light also for the cylindrical micro-object [15]. A non-paraxial Gaussian beam was approximated by a system of rays with the parameters on the same beam shown in Fig. 8.24. A cylindrical object with a diameter of $1\ \mu\text{m}$ and a refractive index of 1.41 was shifted across the axis of the Gaussian beam, with the values of the forces F_x and F_y calculated in each position. Figure 8.24 shows approximation of a Gaussian beam by a system of rays and refraction of the rays by this system at different positions of the cylindrical micro-object with respect to the optical axis.

For a cylindrical micro-object we calculated the force of light in the Gaussian beam. Figure 8.25a is a plot of the dependence of the projections of the force F_z on the displacement with respect to the waist along the propagation axis of the beam, superimposed on the graph presented in Section 8.1. Figure 8.25b is a plot of the dependence of projections of force F_y on the displacement relative to the axis of beam propagation, superimposed on the graph presented in Section 8.1 [7–9].

For the longitudinal force (Fig. 8.25a) there is an area where the standard deviation of force, obtained in the geometrical optics approximation, from the force calculated in the framework of the electromagnetic approach is no more than 0.1. As seen in Fig. 8.25b, for the shear force there is also a region in which the standard deviation is not more than 0.1.

To determine the accuracy, a standard formula was used for calculating the standard deviation (S.K.O.):

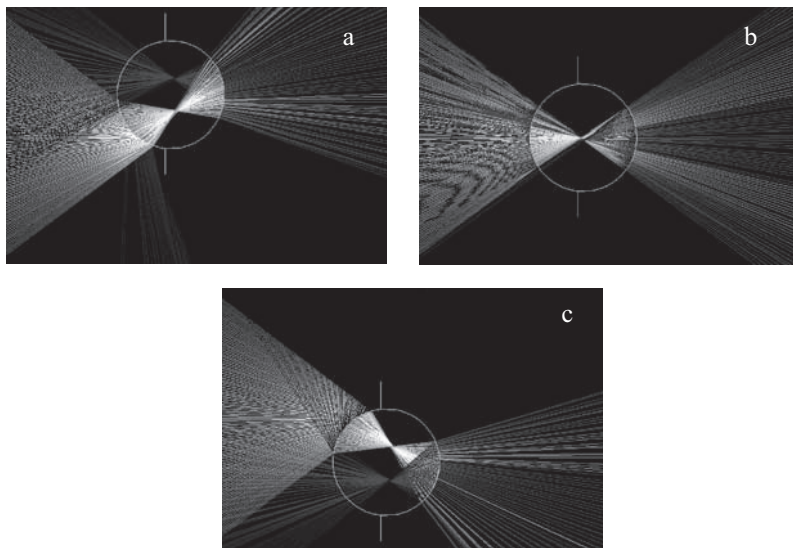


Fig. 8.24. Refraction of beams on a cylindrical micro-object $1 \mu\text{m}$ in diameter in different positions relative to the beam axis, (a) the displacement by $0.5 \mu\text{m}$ upwards, (b) exactly on the beam axis, (c) the displacement by $0.5 \mu\text{m}$ downward.

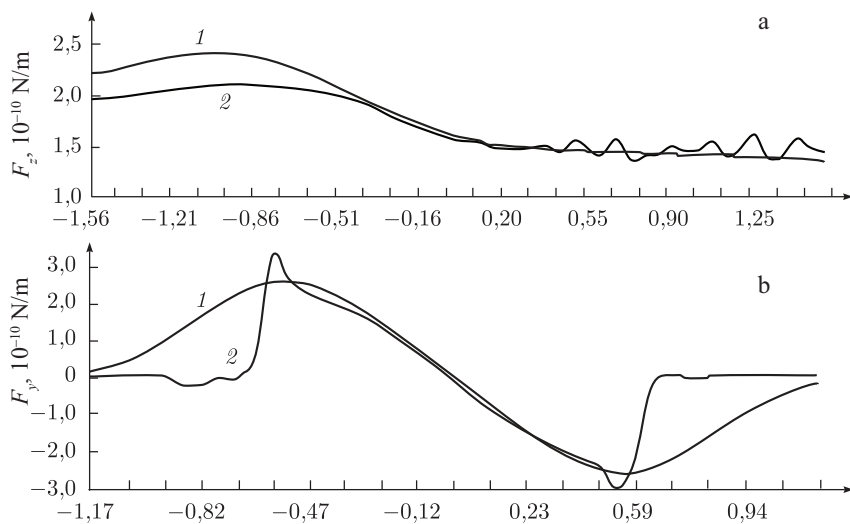


Fig. 8.25. a) The dependence of force F_z on the displacement L of the object along the Z axis through the centre of the waist ($Y = 0$), b) dependence of force F_y on the displacement L of the object along the Y axis through the centre of the waist ($Z = 0$) (1 – exact calculation, 2 – calculation by geometrical optics .)

$$\sigma = \frac{\sqrt{\frac{1}{N} \sum_{i=1}^N (f_{1i} - f_{2i})^2}}{\langle f_2 \rangle}, \quad (8.26)$$

where f_{1i} is the sampling point of the compared function, f_{2i} is the discretization point of the reference function, N is the number of discretization points of the function, $\langle f_2 \rangle$ is the mean value of the reference function.

These results suggest that the geometrical optics method for calculating the forces acting on the micro-object from the light beam has the error of no more than 0.1, except in cases of no practical interest, such as displacement of more than 0.5 μm from the beam axis in Fig. 8.25b. In this case, the method has a much lower computational complexity than the exact methods of calculation, which allows not only to calculate the forces acting on the micro-object in the light field, but also to simulate the motion of the micro-object.

8.4. Rotation of micro-objects in a Bessel beam

8.4.1. Transformation of diffractionless Bessel beams

In optical systems for the rotation of micro-objects with the help of a Bessel beam (BB) [28, 52, 73, 92] the light energy is concentrated using a ring BB ‘squeezed’ through a spherical lens. However, it appears that BB has the property to maintain its diameter near the axicon or DOE, loses this property in imaging using a spherical lens and begins to disperse.

We show that the image of the diffractionless BB produced using with a spherical lens leads to a divergent BB. Figure 8.26 shows the optical scheme.

As an initial function we choose the zero-order Bessel beam:

$$\Psi_0(r) = J_0(\alpha r). \quad (8.27)$$

To find how the function Ψ_0 is transformed by a lens, we need to simulate the passage of the beam in free space over distance a by Fresnel transform, then multiply by the complex transmission function of the lens with a focal length f , and again apply the Fresnel transform at distance z :

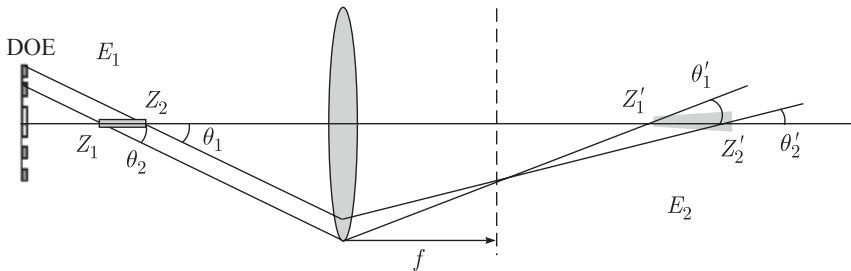


Fig. 8.26. The optical circuit for imaging the Bessel beam, used to manipulate microscopic objects.

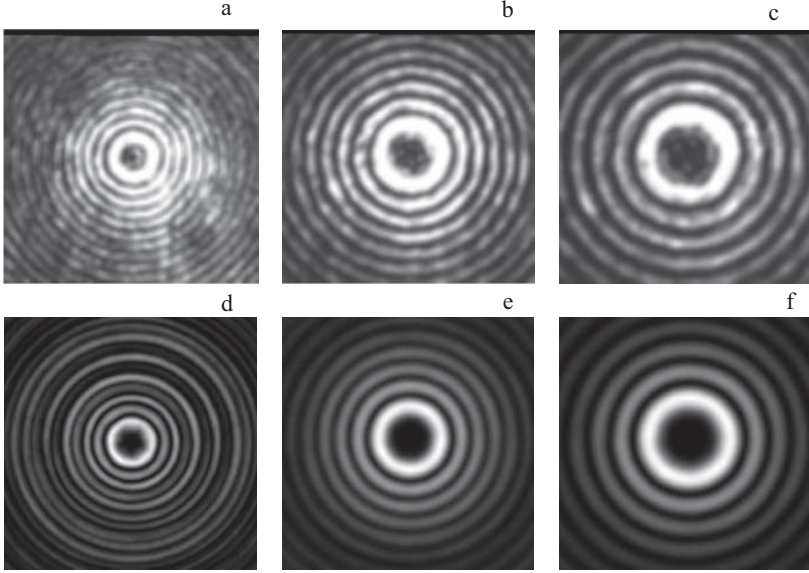


Fig. 8.27. The divergent paraxial Bessel beam at distances of 100 mm, 125 mm, 150 mm, respectively (a), (b), (c) (experiment), (d), (e), (f) (theory).

$$\Psi(u, v, z) = \left(\frac{k}{2\pi i}\right)^2 \frac{1}{az} \times \int_{-\infty}^{\infty} \int_{-\infty}^{\infty} \int_{-\infty}^{\infty} \Psi_0(r) \exp\left\{\frac{ik}{2}\left[\frac{(x-\xi)^2}{a} + \frac{(y-\eta)^2}{a} - \frac{\xi^2 + \eta^2}{f} + \frac{(\xi-y)^2}{z} + \frac{(\eta-v)^2}{z}\right]\right\} dx dy d\xi d\eta. \quad (8.28)$$

The distance z is related to the distance a by the lens formula. Equation (8.28) uses the transmission function of the paraxial lens in the form of:

$$\tau(\xi, \eta) = \exp\left[-\frac{ik}{2f}(\xi^2 + \eta^2)\right]. \quad (8.29)$$

The evaluation of the integral (8.28) we get:

$$\Psi(\rho, z) = \frac{f}{(z-f)} J_0\left(\frac{\alpha f \rho}{f-z}\right) \exp\left[-i\frac{\alpha^2}{2k}\left(a + \frac{fz}{f-z}\right) + i\frac{k\rho^2}{2(f-z)}\right], \quad (8.30)$$

where $\rho^2 = u^2 + v^2$.

Equation (8.30) shows that the BB (8.27) like the non-paraxial beam diverges for $z > f$. This is due to the fact that the lens produces a divergent parabolic wave front in the BB. On the contrary, ??? of the focal plane of the lens converge???

Figure 8.27 shows the results of the experiment compared with the theoretical results for the Bessel function of the fifth order; the experiments were carried out used a lens with a focal length $f = 50$ mm, the distance from the DOE to the lens 200 mm, a He-Ne laser with a wavelength of $0.633 \mu\text{m}$.

Figure 8.27 shows a qualitative agreement between theory and experiment.

It may seem that when imaging with a lens, the diffractionless BB (8.27) becomes a divergent BB (8.30) due to the fact that it was calculated using the paraxial Fresnel transformation. But it is not so. It can be shown that the use of Fresnel transformation for BB (8.27) retains its diffractionless nature. Indeed, we choose as the initial light field the BB in the form:

$$\Psi_0(r, \varphi, z = 0) = J_n(\alpha r) \exp(in\varphi), \quad (8.31)$$

Then at a distance z from the plane $z = 0$, we obtain:

$$\Psi(\xi, \eta, z) = \frac{k}{2\pi iz} \int_0^\infty \int_0^{2\pi} J_n(\alpha r) \exp(in\varphi) \exp\left[\frac{ik}{2z}(r^2 + \rho^2)\right] \exp\left[-\frac{ik}{z}r\rho \cos(\theta - \varphi)\right] r dr d\varphi, \quad (8.32)$$

where $\rho^2 = \xi^2 + \eta^2$, $\theta = \arctg(\eta/\xi)$.

Replacing the integral with respect to φ (8.32) by the Bessel function of the n -th order, instead of (8.32) we get:

$$\Psi(\rho, \theta, z) = \frac{(-i)^{n+1} k}{z} \exp\left(\frac{ik}{2z}\rho^2\right) \exp(in\theta) \int_0^\infty J_n(\alpha r) J_n\left(\frac{kr\rho}{z}\right) \exp\left(\frac{ik}{2z}r^2\right) r dr. \quad (8.33)$$

The integral in (8.33) can be calculated, then instead of (8.33) we get:

$$\Psi(\rho, \theta, z) = \exp\left(-i\frac{z\alpha^2}{2k}\right) J_n(\alpha\rho) \exp(in\theta). \quad (8.34)$$

From (8.34) shows that the Fresnel transformation preserves the original paraxial non-diverging BB (with the accuracy up to a phase factor) [19, 62]:

$$\Psi(\rho, \theta, z) = \exp\left(-i\frac{z\alpha^2}{2k}\right) \Psi_0(\rho, \theta). \quad (8.35)$$

Thus, in this section it is shown that the paraxial BB keeps its diameter in propagation in space, but converts into convergent and divergent light BB with a spherical lens. This property of BB should be considered in optical manipulation of micro-objects.

8.4.2. Umov–Poynting vector for a non-paraxial 2D vector Bessel beam

In the two-dimensional case we obtain a simpler relation between the scalar and vector BBs. In the two-dimensional case, the expansion of a complex function satisfying the Helmholtz equation in plane waves has the form [75]:

$$\Psi(x, z) = \int_{-\infty}^{\infty} \Psi_0(t) \exp \left[ik \left(xt + z\sqrt{1-t^2} \right) \right] dt, \quad (8.36)$$

where z is optical beam axis (on the y -axis there are no changes $\partial/\partial y = 0$).

If we select $\Psi_0(t)$ in the form of:

$$\Psi_0(t) = \frac{(-i)^n \exp \left[in \arccos \left(\frac{t}{a} \right) \right]}{2\pi \sqrt{a^2 - t^2}} \operatorname{rect} \left(\frac{t}{a} \right), \quad (8.37)$$

then substituting (8.37) into (8.36) we obtain an expression for the non-paraxial two-dimensional beam which at $z = 0$ coincides with the Bessel beams:

$$\Psi(x, z) = \frac{(-i)^n}{2\pi} \int_{-a}^a \frac{\exp \left[in \arccos \left(\frac{t}{a} \right) \right]}{\sqrt{a^2 - t^2}} \exp \left[ik \left(xt + z\sqrt{1-t^2} \right) \right] dt. \quad (8.38)$$

From Eq. (8.38) at $z = 0$ and after the change $t = a \cos \varphi$, we obtain

$$\Psi(x, z = 0) = \frac{(-i)^n}{2\pi} \int_0^\pi \exp(in\varphi) \exp(ika \cos \varphi) d\varphi = J_n(kax). \quad (8.39)$$

To get a compact notation for the Bessel beam at any z we can write Eq. (8.36) as

$$\Psi(x, z) = \int_{-\pi}^{\pi} \Psi_0(\theta) \exp \left[ik(x \cos \theta + z \sin \theta) \right] d\theta. \quad (8.40)$$

Then, for

$$\Psi_0(\theta) = \frac{(-i)^n}{2\pi} \exp(in\theta), \quad (8.41)$$

instead of (8.38) we obtain

$$\Psi(x, z) = \frac{(-i)^n}{2\pi} \int_{-\pi}^{\pi} \exp(in\theta) \exp \left[ik(x \cos \theta + z \sin \theta) \right] d\theta = J_n(kr) \exp(in\varphi), \quad (8.42)$$

where $x = r \sin \varphi$, $y = r \cos \varphi$.

At $z = 0$ from Eq. (8.42) we get:

$$\Psi(x, z = 0) = J_n(kr) (i \operatorname{sgn} x)^n. \quad (8.43)$$

The scalar two-dimensional Bessel beam (8.42) can be regarded as a vector beam, assuming that $\Psi(x, z)$ is the projection on the y -axis of the vector of the

electric field $E_y(x, z) = \Psi(x, z)$ for the TE-polarized monochromatic electromagnetic wave. This field is described by three quantities E_y, H_x, H_z , where H_x and H_z are the projections on the x and z axes of the vector of the strength of the magnetic field of the wave. Projections of the magnetic vector can be found through E_y :

$$\begin{aligned} H_x &= \frac{1}{ik} \frac{\partial E_y}{\partial z}, \\ H_z &= \frac{i}{k} \frac{\partial E_y}{\partial x}. \end{aligned} \quad (8.44)$$

With the help of equations (8.42) and (8.44) we can find an expression for the Umov–Poynting vector of the two-dimensional Bessel beam. Indeed, the Umov–Poynting vector is defined for complex vector fields in the form:

$$\mathbf{S} = \frac{c}{4\pi} \operatorname{Re} \left[\mathbf{E} \times \mathbf{H}^* \right], \quad (8.45)$$

where c is the speed of light.

In two dimensions, taking into account (8.42), instead of (8.44) we get:

$$S_x = \frac{ic}{4\pi k} \left(E_y \frac{\partial E_y^*}{\partial x} - E_y^* \frac{\partial E_y}{\partial x} \right) = \frac{c}{4\pi k} \operatorname{Im} \left(E_y \frac{\partial E_y^*}{\partial x} \right), \quad (8.46)$$

$$S_z = \frac{ic}{4\pi k} \left(E_y \frac{\partial E_y^*}{\partial z} - E_y^* \frac{\partial E_y}{\partial z} \right) = \frac{c}{4\pi k} \operatorname{Im} \left(E_y \frac{\partial E_y^*}{\partial z} \right). \quad (8.47)$$

Substituting (8.42) into (8.46) and (8.47), we obtain the projection of the Umov–Poynting vector for the two-dimensional Bessel beam with TE polarization

$$S_x(x, z) = \frac{cnz}{4\pi k r^2} J_n^2(kr), \quad (8.48)$$

$$S_z(x, z) = \frac{-cnx}{4\pi k r^2} J_n^2(kr). \quad (8.49)$$

From equations (8.48) and (8.49) it follows that at $z = 0$ $S_x(x, z = 0) = 0$ and

$$S_z(x, z = 0) = \frac{-cn}{4\pi kx} J_n^2(kx), \quad (8.50)$$

and at $x = 0$, $S_z(x = 0, z) = 0$ and

$$S_x(x = 0, z) = \frac{cn}{4\pi kz} J_n^2(kz). \quad (8.51)$$

Arrows in Fig. 8.28 indicate the direction of the Umov–Poynting vector, which follows from equations (8.48)–(8.51).

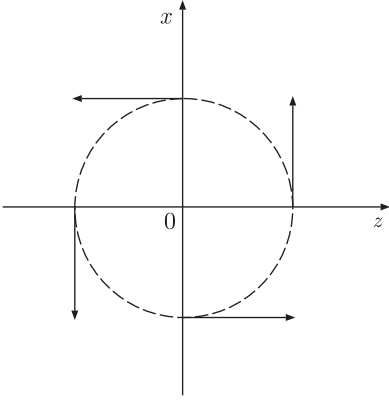


Fig. 8.28. The arrows indicate the direction of the Umov–Poynting vector at $r = \text{const}$ for a 2D Bessel beam of the n -th order.

8.4.3. Umov–Poynting vector for the paraxial 3D vector Bessel beam

Let a monochromatic Bessel beam be linearly polarized along axis x :

$$\mathbf{E} = \mathbf{e}_x U(x, y, z) = \mathbf{e}_x J_n(\alpha r) \exp[i(\beta z + n\varphi)], \quad (8.52)$$

where $\alpha = k \sin \theta$, $\beta = k \cos \theta$, θ is the angle of the conical wave to the optical axis z , (r, φ) are the polar coordinates. From Maxwell's equations

$$\begin{cases} \text{rot } \mathbf{E} = ik\mathbf{H}, \\ \text{rot } \mathbf{H} = -ik\varepsilon\mathbf{E}. \end{cases} \quad (8.53)$$

We find the rest of the projection of the electric and magnetic vectors:

$$\begin{cases} E_x = U, \\ E_y = \frac{1}{k^2 \varepsilon} \frac{\partial^2 U}{\partial y \partial x}, \\ E_z = \frac{1}{k^2 \varepsilon} \frac{\partial^2 U}{\partial z \partial x}, \end{cases} \quad \begin{cases} H_x = 0, \\ H_y = \frac{1}{ik} \frac{\partial U}{\partial z}, \\ H_z = \frac{i}{k} \frac{\partial U}{\partial y}. \end{cases} \quad (8.54)$$

It is seen that the projection H_y and H_z of the order k^{-1} , and E_y and E_z of the order k^{-2} , i.e. small compared with E_x .

The Umov–Poynting vector is defined by equation (8.45) with (8.54) takes the form:

$$S_z = \frac{c}{4\pi k} \text{Im} \left[U^* \frac{\partial U}{\partial z} \right], \quad (8.55)$$

$$S_y = \frac{c}{4\pi k} \text{Im} \left[U^* \frac{\partial U}{\partial y} \right], \quad (8.56)$$

$$S_x = \frac{c}{4\pi \epsilon k} \text{Im} \left[\frac{\partial^2 U}{\partial y \partial x} \frac{\partial U^*}{\partial y} + \frac{\partial^2 U}{\partial z \partial x} \frac{\partial U^*}{\partial y} \right]. \quad (8.57)$$

We substitute the expression for U from (8.52) into (8.55)–(8.57) and obtain the projection of the Umov–Poynting vector of the 3D vector paraxial Bessel beam:

$$S_z = \frac{c\beta}{4\pi k} J_n^2(\alpha r), \quad (8.58)$$

$$S_y = \frac{cnx}{4\pi kr^2} J_n^2(\alpha r), \quad x = r \cos \varphi, \quad (8.59)$$

$$\begin{aligned} S_x = & \frac{-cn}{4\pi k\epsilon} \left\{ \left(\frac{\beta^2 y}{k^2 r^2} + \frac{n^2 x^2 y}{k^2 r^6} \right) J_n^2(\alpha r) - \right. \\ & - \left(\frac{\alpha y}{k^2 r^3} - \frac{2\alpha x^2 y}{k^2 r^5} + \frac{\alpha xy^2}{k^2 r^5} \right) J_n(\alpha r) \frac{\partial J_n(t)}{\partial t} + \\ & \left. + \left(\frac{\alpha^2 y^3}{k^2 r^4} - \frac{\alpha^2 x^2 y}{k^2 r^4} \right) \left(\frac{\partial J_n(t)}{\partial t} \right)^2 + \frac{\alpha^2 x^2 y}{k^2 r^4} J_n(\alpha r) \frac{\partial^2 J_n(t)}{\partial t^2} \right\}. \end{aligned} \quad (8.60)$$

Note that equation (8.58) and (8.59) are similar and almost identical with the equations (8.49) and (8.48), respectively.

If in (8.60) we leave only the terms proportional to k^{-1} , and the terms with k^{-2} and k^{-3} ignored, instead of (8.60), we obtain a simple expression:

$$S_x = \frac{-cn}{4\pi k\epsilon} \left\{ \frac{\beta^2 y}{k^2 r^2} J_n^2(\alpha r) + \left(\frac{\alpha^2 y^3}{k^2 r^4} - \frac{\alpha^2 x^2 y}{k^2 r^4} \right) \left(\frac{\partial J_n(t)}{\partial t} \right)^2 + \frac{\alpha^2 x^2 y}{k^2 r^4} J_n(\alpha r) \frac{\partial^2 J_n(t)}{\partial t^2} \right\}. \quad (8.61)$$

From Eq. (8.58)–(8.60) we see that at $x = 0$:

$$\begin{cases} S_y = 0, \\ S_x = \frac{-cn}{4\pi k\epsilon} \left[\frac{\beta^2 y}{k^2 r^2} J_n^2(\alpha r) + \frac{\alpha^2 y^3}{k^2 r^4} \left(\frac{\partial J_n(t)}{\partial t} \right)^2 \right]. \end{cases} \quad (8.62)$$

The sign S_x is determined by the product ny , with $n > 0$ and at $r = \text{const}$ projection S_x is aimed at in Fig. 8.29 (z -axis is directed toward the observer).

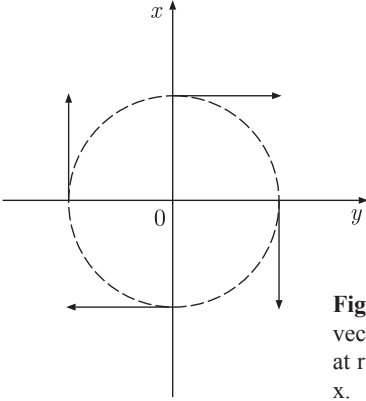


Fig. 8.29 The arrows indicate the direction of the Poynting vector in the cross section (x, y) 3D paraxial Bessel beam at $r = \text{const}$. The light is linearly polarized along the axis x .

At $y = 0$:

$$\begin{cases} S_x = 0, \\ S_y = \frac{cnx}{4\pi kr^2} J_n^2(\alpha r). \end{cases} \quad (8.63)$$

The sign S_y is determined by the product nx and for $n > 0$ the projection is shown in Fig. 8.29.

8.4.4. The orbital angular momentum for a Bessel beam

The orbital angular momentum of the electromagnetic field is given by [27]:

$$\mathbf{M} = [\mathbf{r} \times \mathbf{S}] = \left[\mathbf{r} \times \left\{ \frac{c}{4\pi} \text{Re}[\mathbf{E} \times \mathbf{H}] \right\} \right]. \quad (8.64)$$

The projection on the optical axis of the orbital angular momentum for a linearly polarized electromagnetic field calculated in the paraxial approximation has the form:

$$M_z = \frac{1}{4\pi kc} \left[y \text{Im} \left(E \frac{\partial E^*}{\partial x} \right) - x \text{Im} \left(E \frac{\partial E^*}{\partial y} \right) \right]. \quad (8.65)$$

For a linearly polarized Bessel beam

$$E_x = J_n(\alpha r) \exp(in\varphi) \exp(i\beta z), \quad \alpha^2 + \beta^2 = k^2 \quad (8.66)$$

projection on the z axis of the orbital angular momentum will be:

$$M_z = \frac{nJ_n^2(\alpha r)}{4\pi kc}. \quad (8.67)$$